Microstructure Characterization of As-cast, Creep-tested and Ex-service Steam-methane Reformer Tube

by

Nurul Aini Binti Mohd Faudzi

Dissertation submitted in partial fulfilment of
the requirements for the
Bachelor of Engineering (Hons)
(Mechanical Engineering)

JANUARY 2009

Universiti Teknologi PETRONAS
Bandar Seri Iskandar
31750 Tronoh
Perak Darul Ridzuan

CERTIFICATION OF APPROVAL

Microstructure Characterization of As-cast, Creep-tested and Ex-service Steam-methane Reformer Tube

by

Nurul Aini Binti Mohd Faudzi

A project dissertation submitted to the
Mechanical Engineering Programme
Universiti Teknologi PETRONAS
in partial fulfilment of the requirement for the
BACHELOR OF ENGINEERING (Hons)
(MECHANICAL ENGINEERING)

Approved by,

_____
(Dr. Azmi Bin Abdul Wahab)

UNIVERSITI TEKNOLOGI PETRONAS

TRONOH, PERAK

January 2009

CERTIFICATION OF ORIGINALITY

This is to certify that I am responsible for the work submitted in this project, that the original work is my own except as specified in the references and acknowledgements, and that the original work contained herein have not been undertaken or done by unspecified sources or persons.

_____

NURUL AINI BINTI MOHD FAUDZI

ABSTRACT

The main objective of this project is to study the microstructural transformation of a steam-methane reformer tube material during creep and after long term service by comparing the microstructures in creep-tested samples, ex-service samples, and as-cast samples. The creep-tested samples were not completely representative of the actual creep process during service. The ex-service material represents the material that underwent actual service condition. The as-cast and creep-tested samples were obtained from the Schmidt+Clemens (Spain) for preparation and evaluation, while the ex-service samples were obtained from a methanol plant in North America. The microstructural comparisons were made in terms of the shape, average particle size, particle area fraction and percentage. The samples were examined using optical microscope (OM) and scanning electron microscope (SEM), with secondary electron (SE) and backscattered electron (BSE) imaging. Energy dispersive spectroscopy (EDS) was conducted at selected areas of the samples. The average particle size and particle area percentage of the primary carbides were measured using NIH ImageJ software. The shape of the primary carbides ($M_{23}C_6$ and NbC) in the ex-service sample is rounder compared to the creep-tested and finer shape of the as-cast sample with increasing service time and temperature.

ACKNOWLEDGEMENT

Firstly, the highest gratitude goes to Allah the Al-Mighty. Next, the author would like to express humble gratitude to the author's family, FYP's supervisor, Dr. Azmi Bin Abdul Wahab, UTP's technicians, Mr. Zamil, Mr. Faisal, Mr. Anuar, and Mr. Irwan, and friends all over. These people have helped the author a lot to successfully complete this project within the time provided. It has been a wonderful time working together and the author has learned a lot in a short period of time.

As an undergraduate, it is important for the author to have a positive mind set during this period so as to avoid bad habits such as laziness and procrastination. Throughout the two semesters, the author has gained a valuable experience in various aspects especially in engineering materials. The exposure to such environment will be very useful to the author's future career. The author hope to make good use of the knowledge gained.

Personally, this is a great experience as the author was allowed to be involved with hands-on tasks throughout these two semesters. The author hope that all the information gained from this project may benefit others especially the UTP's students and staffs as a source of reference.

TABLE OF CONTENTS

LIST OF FIGURES

LIST OF TABLES

LIST OF APPENDIX

ABBREVIATION

The following abbreviations are used throughout this document:

ASTM	American Society of Mechanical Engineers
BSE	Backscattered Electron
EDS	Energy Dispersive Spectroscopy
EDM	Electrical Discharge Machining
OM	Optical Microscope
RAM	Random Access Memory
SE	Secondary Electron
SEM	Scanning Electron Microscope
SMR	Steam-methane Reformer

CHAPTER 1

INTRODUCTION

1. BACKGROUND OF STUDY

In petrochemical plants, the production of hydrogen from natural gas is carried out in hydrogen reformers or also known as steam-methane reformers, where the following reactions occur in the presence of a nickel catalyst:

$$CH_4 + H_2O \rightarrow CO + 3H_2$$

$$CO + H_2O \rightarrow CO_2 + H_2$$

The steam-methane reformers consist of hundreds of vertically oriented straight tubes with an internal diameter and wall thickness of about 125mm and 10mm respectively. Each tube consists of three segments with a length of 4.5m each, thus the total length is 13.5m. During plant operation, these tubes are filled with catalyst while gasses pass through at extremely high temperature of more than 900°C and an internal pressure of approximately 2MPa. Hence, these tubes are susceptible to a failure mechanism referred to as “creep” [1].

Before reformer tubes can be used at high temperatures, they usually underwent creep testing procedures. Several samples of the creep-tested reformer tubes are then obtained to characterize the microstructure for full understanding on its material behaviour. The creep-tested samples were not completely representative of the actual creep process

during service. The ex-service material represents the material that underwent actual service condition [3].

In recent years, the experimental procedures for characterizing the microstructure, including phase identification, the morphology of primary and secondary precipitates, as well as studies of phase transformation have been well developed and reported in the literature. However, a review of the results contained in more recently published papers dealing with steam-methane reformer tube material indicate that these characterization techniques should be discussed further in order to clarify their capabilities for the identification of phases and transformation mechanisms. These characterization methods would also contribute to an understanding of the role of additive elements in developing improved mechanical properties [3].

1.1 Problem Statement

Steam-methane reformer tubes are designed to last about 100,000 hours of service. However, strength and performance of these tubes in service are based on 1,000 hours of creep tests. Hence, the microstructures present within the material for 1,000 hours and 100,000 hours may be different, perhaps due to a more rapid “ageing” process during the creep tests as compared to the lengthy operating period. The differences in microstructure in creep-tested material and in service material have not been properly documented [2].

1.2 Objective

The main objective of this project is to characterize and compare the microstructures of the as-cast, creep-tested, and ex-service steam-methane reformer tube material. The microstructures are to be investigated in terms of precipitate types, shape, average particle size, particle area fraction and percentage, and any additional microstructure formed. The results are to be discussed with respect to the current practice of

performing accelerated creep tests and using time-temperature parameters for the life estimates [2].

1.3 Scope of Study

Several tube samples were supplied for analysis. These were taken from the reformer tubes in the plant. The samples data are given in the nomenclature and operating conditions section. The O1 sample is an as-cast sample from a new reformer tube made from Schmidt+Clemens CA4852 micro alloy. This sample will be studied for comparison and act as a base microstructure. Samples A1, A2 and A3 are the creep-tested samples tested at different conditions, A1 at 1030°C, A2 at 1020°C, and A3 at 1010°C.

Samples K1, K2 and K3 are the ex-service samples. All of the samples can be expected to exhibit significantly different microstructures. Temperature for K1 is higher than K2 and K3. Sample K3 experienced higher pressure than K2 and K1. Significant evidence of ageing was expected [14].

Above all, this study concentrates on one type of alloy although there are many types of alloys being used to manufacture reformer tubes. Therefore, the findings are limited to the Schmidt+Clemens CA4852 micro alloy from Spain. Hence, the work done in this project was only one part of the bigger picture that could represent the behaviour and effect of creep to reformer tube.

CHAPTER 2

LITERATURE REVIEW

2. STEAM-METHANE REFORMER

On an industrial scale, steam-methane reforming is a dominant method for producing hydrogen. The reason is because this method is least expensive [4]. Steam-methane reformer (SMR) is a device used in petrochemical plant. It produces pure hydrogen gas from hydrocarbon using a nickel-base catalyst at high temperature and high pressure. External source of hot gas is used to heat the reformer tube. During the catalytic reaction, steam and lighter hydrocarbons such as natural gas (methane) or refinery feedstock are converted into hydrogen and carbon monoxide (syngas). The syngas reacts further to give more hydrogen and carbon dioxide in the reactor. The carbon dioxides are removed before usage by means of pressure swing adsorption (PSA), with molecular sieves for the final purification. The pressure swing adsorption will absorb all impurities in the syngas stream. This leaves only pure hydrogen gas [6].

A conventional steam-methane reforming plant operates at pressures between 1.4MPa and 4.1MPa. The usual outlet temperatures are in the range of 815 to 925°C. The capital cost of a steam-methane reforming plant does not scale down well. The applications are prohibitive for small to medium size. Analyses have proved that a well-designed steam-methane reformer can produce hydrogen more cost effectively [6].

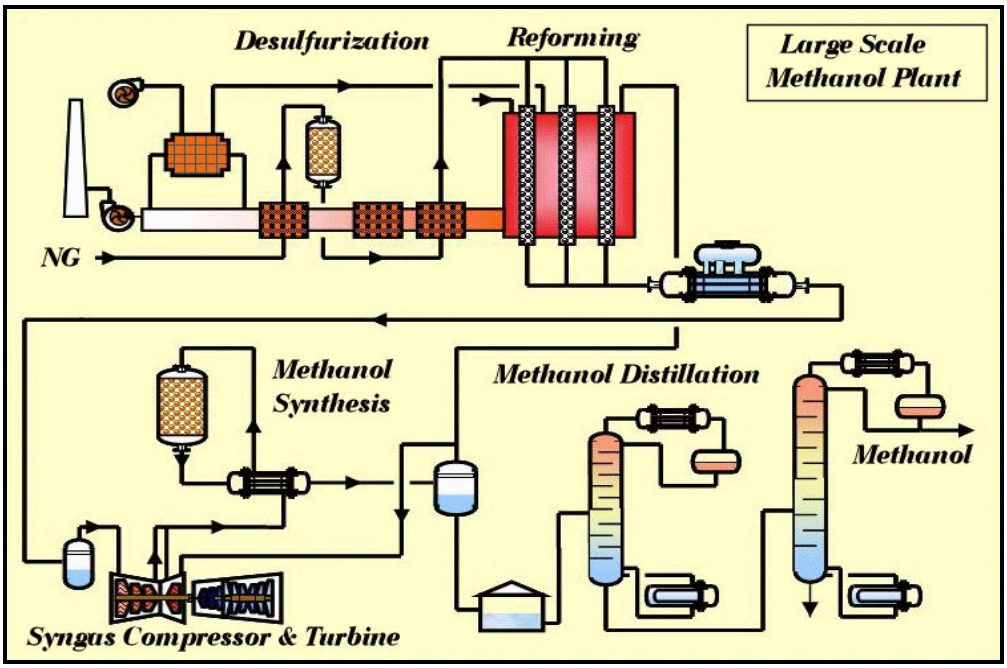

Figure 2.1: SMR process [9].

2.1 Reformer Tubes and Their Use

In steam-methane reformers, there are hundreds of reformer tubes. Each reformer tube is vertically oriented. The inner diameter of each tube is between 76.2mm (3.0in) and 127mm (5.0in). In petrochemical industry, the reformer tube plays an important role. There are more than 1000 tubes in this particular plant in North America. The matter of reformer tube life is one of considerable importance to the industry. Therefore, the costing of the reformer tube can be presented by the amount of capital cost involved. A complete reformer tube change cost around US$ 20,000. Prematurely failed tube forces a plant to shutdown. It will take seven days to replace one reformer tube. Therefore, being able to identify and locate such damage in its early stages of growth is essential for safe and low running cost plant operation. Thus, on occasion, a small number of the tubes are sectioned and analyzed to determine the true extent of the creep damage [7].

These tubes are used in methanol production process where natural gas is passed at high temperature over nickel catalyst located inside the reformer tube, producing crude

methanol. The reformer tube does not have an infinite life. The usual given nominal service life of each tube is approximately 100,000 hours (11.4 years approximately). The maximum operating temperature for the steam reforming applications is 1130°C for the analyzed reformer tube in this report. The tube will be removed from service and replaced when estimated or measured creep damage is too severe to continue to service [14].

2.2 Tube Material and Construction

A stainless steel is an iron-carbon alloy with minimum of 11.5 wt% chromium content. The stainless steel does not stain, corrode or rust as easily as ordinary steel. However, it is not stain-proof. In the aviation industry, a stainless steel is called 'corrosion resistant steel', when the alloy type and grade of a stainless steel are not detailed. Stainless steel can be classified by its crystalline structure.

The alloy analysed in this report is Schmidt+Clemens CA4852 micro alloy from Spain. For this project, the crystalline structure is identified as austenitic. Austenitic comprises over 70% of total stainless steel production [7]. It contains a maximum of 0.15% carbon for a wrought austenitic stainless steel, a minimum of 16% chromium and sufficient nickel and/or manganese to retain an austenitic structure at all temperatures from the cryogenic region to the melting point of the alloy. A cast austenitic stainless steel can have up to 0.55% carbon [2].

Reformer tubes are made from a range of different alloy. These alloys usually belong to a special family of high temperature creep resistant stainless steels, known as H series steels. They generally have very high nickel and chromium contents, high carbon contents and smaller quantities of other alloying elements such as molybdenum, niobium and silicon [14].

2.3 Creep

Creep is the tendency of a solid material to slowly move or deform permanently under the influence of stresses. Creep occurs as a result of long term exposure to levels of stress that are below the yield strength. Creep becomes a concern when evaluating material that operates under high stresses and temperatures. Creep is a time-dependent deformation mechanism. The rate of this deformation is a function of the material properties, exposure time, exposure temperature and applied stress. Sometimes, the deformation may become so large that a component may no longer perform its function. However, creep is more severe in materials that are subjected to heat for a long period and near the material melting point. In addition, creep deformation increases with time. Creep behaviour is usually presented as a creep curve in the form of strain versus time. There are three distinct stages called transient or primary creep, steady-state or secondary creep and accelerating or tertiary creep. Transient creep consists of an initially high strain rate which soon decreases to a constant rate found in steady-state creep. During steady-state creep, the deformation rate remains constant until it enters tertiary creep region. At tertiary creep, the strain rate in this region increases with respect to time until failure [6].

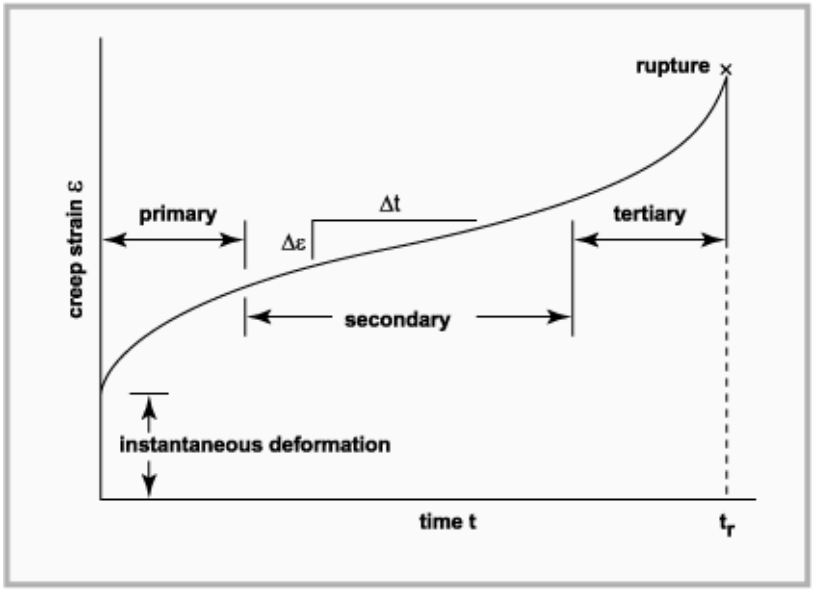

Figure 2.2: Creep curve of strain versus time [6].

The reformer tubes are exposed to harsh environment, elevated temperature and mechanical loading cycles as it is expected to sustain service for more than 100,000 hours (11.4 years). Therefore, they are susceptible to the creep failure mechanism [7].

2.4 Microstructure Characterization

Microstructure characterization scope of work depends on its objectives. It is important for this project because it can give insight about phase identification and transformation mechanism and show the role of additive elements contribute in developing improved mechanical properties. Before characterizing the microstructure, the samples need to be prepared. The method is known as metallographic sample preparation. The objective of this method is to reveal constituents and structure of the metals and their alloys by sampling, sectioning, mounting, grinding, polishing, and etching [7].

During sampling stage, specimen will be selected for preparation. This is to ensure the test sample taken from the parent sample would give representative information. At sectioning stage, large samples will cut into small sizes of samples. The size of the sectioned sample is about 12mm to 25mm (0.5in to 1.0in) square or approximately 12mm to 25mm in diameter if the material is round. Mounting is done for edge preservations by means of hot mounting or cold mounting. The purpose of this stage is for convenience in handling the specimen of difficult shape and sizes during the subsequent steps of metallographic preparation. Grinding is removing of the deformation region induced by the sectioning process by pressing the sample on a rotating piece of abrasive papers. It should start with coarser paper to the finest paper to produce flat surface. At the same time, water is used to wash away debris and also act as lubricant. The final step in producing a deformation-free surface that is flat, scratch free and mirror-like appearance is polishing. It is usually conducted with 6µm or 1µ diamond abrasives charged onto polishing cloths. Lastly, etching is done to further reveal structural aspects such as porosity, cracks, non-metallic inclusions and structural

details of the samples by immersion or swabbing with suitable chemical solution that essentially attack the metal surface [7].

There are two (2) types of microscopes that can be used for the microstructure characterization in this project, namely the optical microscope (OM) and the scanning electron microscope (SEM). The optical microscope is also known as “light optical microscope”. This type of microscope uses visible light and a system of lenses to magnify images of small samples. Optical microscope is usually equipped with various video cameras which allow images to be displayed on high revolution video monitors. The limitation of this microscope is the usable magnification is only up to 1000. For further microstructure characterization, scanning electron microscope can be used to further increase the magnification. Images of sample surface will be produced by scanning with a high-energy beam of electrons. Electrons will interact with the atoms that make up the sample by producing signals that contains sample information. Electron devices are used to detect and amplify signals and display them as an image on a cathode ray tube. The image may be photographed from high resolution cathode ray tube or digitally captured and displayed on a computer monitor. The types of signal made by scanning electron microscope include secondary electrons, characteristics x-rays and backscattered electrons. These signals come from the beam of electrons striking the surface of the specimen and interacting with the sample at or near its surface. In its primary detection mode, secondary electron imaging, the SEM can produce very high-resolution images of a sample surface, revealing details down to about 5nm in size. Due to the way these images are created, SEM micrographs have a very large depth of focus yielding a characteristic three-dimensional appearance useful for understanding the surface structure of a sample. This great depth of field and the wide range of magnifications (commonly from about 25 times to 250,000 times) are available in the most common imaging mode for specimens in the SEM. Characteristic x-rays are the second most common imaging mode for a SEM. X-rays are emitted when the electron beam removes an inner shell electron from the sample, causing a higher energy electron to fill the shell and gives off energy. These characteristic x-rays are used to identify the elemental composition of the sample. Backscattered electrons (BSE)

that come from the sample may also be used to form an image. Backscattered electrons images are often used in analytical SEM along with the spectra made from the characteristics x-rays as clues to the elemental composition of sample [7].

CHAPTER 3

METHODOLOGY

3. PROCEDURE

Figure 3.1 shows the methods applied in this project. Sample preparation stage consisted of sectioning, mounting, grinding, polishing and etching processes. Microstructure observation and image capturing were performed by using OM and SEM. Finally, characterization and data analysis were done by using open source software called NIH ImageJ [7].

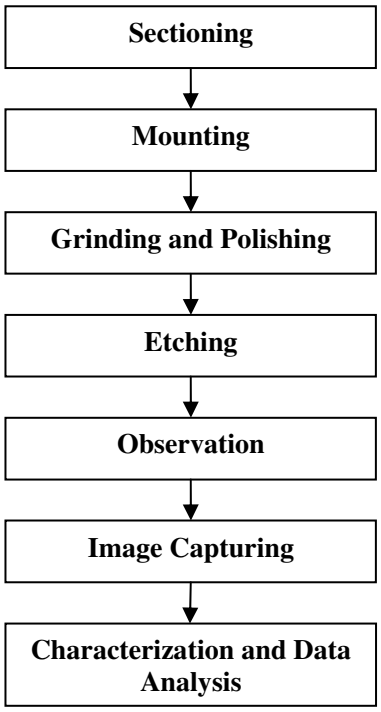

Figure 3.1: Methods involved in the project [7].

3.1 Material Used

Schmidt+Clemens CA4852 micro alloy uses its relatively high niobium content to improve creep rupture strength. The nominal composition of this steel is given in Table 3.1 below. Besides, the mechanical properties of the material are given and tabulated in Table 3.2 [12].

Table 3.1: Specified composition of CA 4852 micro alloy [12].

	C	**Mn**	**Si**	**Cr**	**Ni**	**Nb**	**Ti**	**Fe**
Mass %	0.45	1.0	1.5	25.0	35.0	1.5	Additions	Balance

Table 3.2: Mechanical properties of CA 4852 micro alloy [12].

	200°C	**400°C**	**600°C**	**800°C**	**1000°C**
UTS (MPa)	465	455	380	240	80
YS (MPa)	270	270	230	160	70
El (%)	13	14	17	24	38

Reformer tubes are made via centrifugal casting process. This process involves introducing molten metal into a rapidly rotating cylinder and allowing it to cool. The end result is a large, thick walled tube needing relatively little final processing before being placed into service [14]. The as-cast reformer tube sample that obtained for this work is designated O1.

The reforming process taking place inside the tubes involves an endothermic reaction. It is a process or reaction that absorbs energy in the form of heat. This reaction creates a negative temperature gradient between the outside and the inside walls. This temperature gradient is at highest at the top of the tube and lowest at the bottom.

Figure 3.2 shows the schematic of the creep test sample. The samples were tested and obtained from Schmidt+Clemens. The parameters for the creep tests are shown in Table 3.3. The axial stress remained constant at 23MPa while temperature is varied, resulting in variation in time to rupture. The temperature variation was chosen by Schmidt+Clemens.

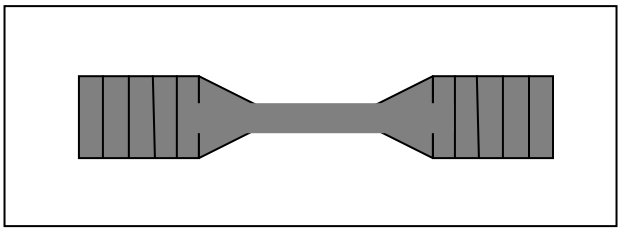

Figure 3.2: Schematic of the creep test sample.

Table 3.3: Operating conditions for creep-tested samples [12].

Samples	**Temperature (°C)**	**Axial Stress, σ (MPa)**	**Time to rupture (hours)**
A1	1030	23	745
A2	1020	23	888
A3	1010	23	1296

Figure 3.3 shows the location of ex-service samples on the tube. The corresponding temperatures at these locations were obtained from a methanol plant in North America and shown in Table 3.4. It is understood that the actual operating temperatures might in fact be slightly higher than this. It is also believed that the hoop stress caused by this pressure is much lower than the thermally induced stress [14].

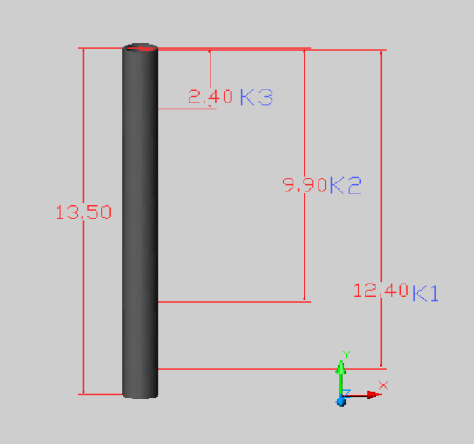

Figure 3.3: Location of ex-service tube section (in meters, m).

Table 3.4: Operating conditions for ex-service samples [12].

Samples	Depth from Top (m)	Service Length (hours)	Temperature (°C)
K1	12.4	90, 000	890
K2	9.9	90, 000	870
K3	2.4	90, 000	730

3.2 Sample Preparation

The samples were prepared to produce a mirror like surface to analyze the materials microstructures. The sample preparation consisted of sectioning, mounting, grinding, polishing and etching processes [7].

3.2.1 Sectioning

Sectioning is the removal of a representative sample from the parent piece by removing a suitably sized specimen at desired location and orientation. The sectioning plane should be as near as to the desired location as possible [7]. Electrical Discharge

Machining (EDM) machine was used for precise sectioning, and also to ensure that the microstructure was not altered in the process.

Figure 3.4 shows the parent piece and samples that had been sectioned. In this project, all the samples obtained were sectioned in the longitudinal plane of the parent sample. The average dimension of each sectioned sample was 15mm (length), 7mm (width), and 10mm (thickness).

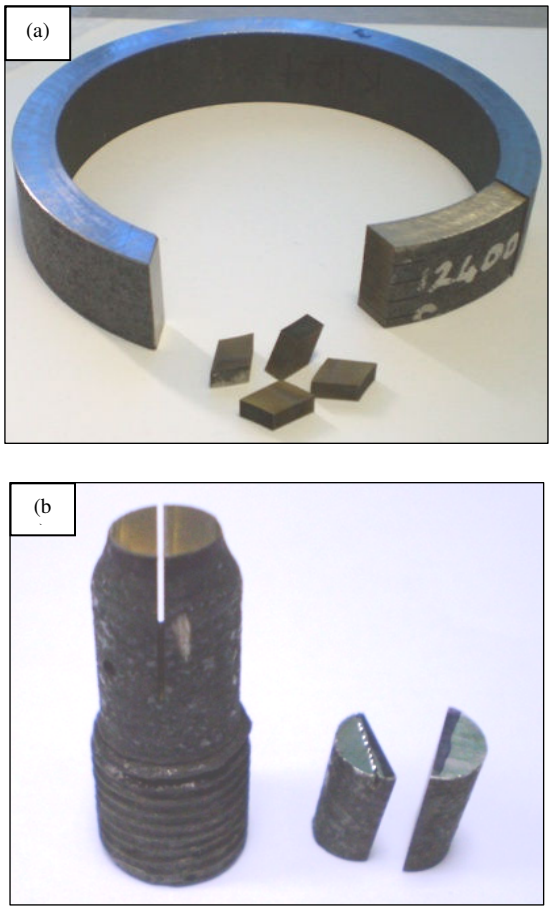

Figure 3.4: (a) Ex-service sample, (b) Creep-tested sample.

3.2.2 Mounting

The main purpose of mounting metallographic specimens is for convenience in handling specimens of difficult shapes or sizes during the subsequent steps of

metallographic preparations and examinations. Besides, mounting process will protect and preserve extreme edges or surface defects during metallographic preparation [7].

There are two types of mounting methods that can be applied, that is cold and hot mounting. Cold mounting will be performed with a mixture of resin and hardener. Hot mounting uses a certain amount of pressure and heat to mount the samples. In this project, hot mounting was applied and it would not affect the microstructures of the samples because the range of the temperature of the mounting process is from 140°C to 160°C, which is only a fraction of the reformer tube operating temperature of 800°C to 900°C. Below is listed the hot mounting equipment, material, and parameters [7].

- Equipment : SIMPLIMENT 1000, AUTOMATIC MOUNTING PRESS
- Powder : Bakelite green or black powder
- Heat time : 2 minutes
- Cool time : 5 minutes
- Temperature : 140°C to 160°C
- Pressure : 4200 psi or 29MPa

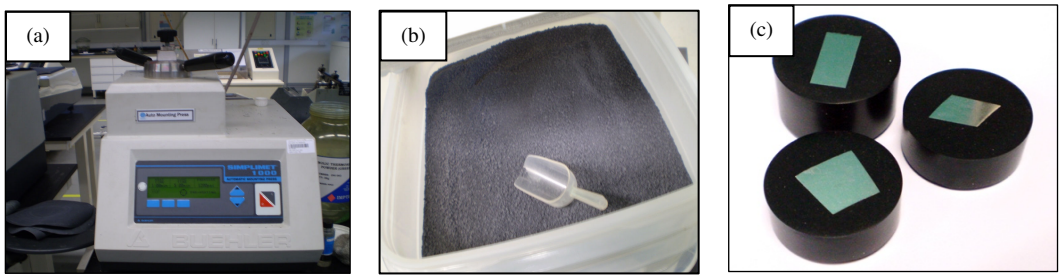

Figure 3.5: (a) Hot mounting equipment, (b) Bakelite powder, (c) Mounted samples.

3.2.3 Grinding and Polishing

Figure 3.6 shows the grinding and polishing equipment. Grinding can be divided into two parts. Coarse grinding produces an initial flat surface and fine grinding remove the zone of deformation due to sectioning and coarse grinding. The depths of deformation

during the grinding and polishing stage can be limited by proper abrasive size sequencing. All of the grinding steps will be performed with water as lubricant. Moreover, water also minimized specimen heating and prevented the abrasive from becoming loaded with metal removed from the specimen being prepared [7].

The final step in producing a deformation-free surface that is flat, scratch free and mirror-like in appearance is polishing. This step involves observation of the true microstructure for subsequent metallographic interpretation, both qualitative and quantitative. Polishing can be divided into two parts. Rough polishing is a further limitation of the deformation zone produced by fine grinding and final polishing is to remove the deformation zone produced during rough polishing [7].

The samples underwent grinding steps as shown in the Table 3.5. The polishing steps were done with 6 and 1µm diamond paste charged onto a low nap cloth. A control sample was also prepared from an as-cast tube made from the same alloy to compare the microstructures with the microstructures of the creep-tested and ex-service samples [7].

Table 3.5: SiC grit size and proposed wheel speed for grinding.

SiC Grit Size	Wheel Speed (RPM)
320	100 - 250
400	100 - 250
600	100 - 250
800	100 - 250

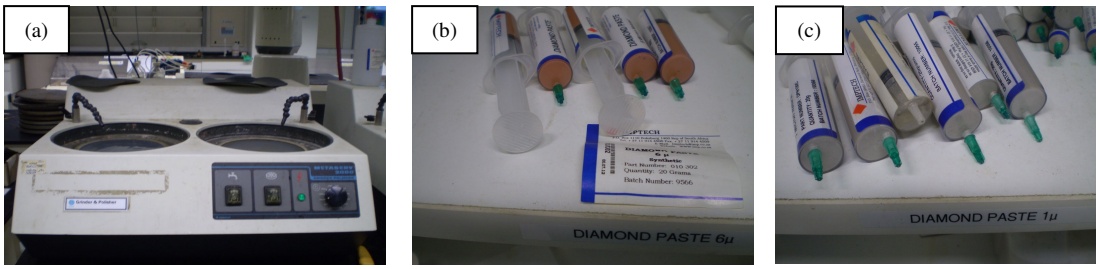

Figure 3.6: (a) Equipment, (b) 6µm diamond paste, (c) 1µm diamond paste.

3.2.4 Etching

All preparation and etching processes is to be referred from the ASTM Standards Volume 3.01 designated in section E381-94 titled Standard Method of Macroetching and E407-99 titled Standard Practice for Microetching Metals and Alloys. Etching is the process to reveal structural details by preferential attack of a metal surface with an acid of basic chemical solution to reveal inclusions, porosity, cracks, intergranular corrosion and details of the samples. The samples in this project were etched in glyceregia. It is important to note that glyceregia could not be stored for a period of time due to the degradation over time and there is also a potential of glyceregia becoming very reactive over time. Table 3.6 shows the glyceregia composition, reaction type and methods to be applied in this project [7].

Table 3.6: Etchants to be used on the Austenitic Stainless Steel.

	Composition	**Type**	**Method**
Glyceregia	10ml Glycerol, 15ml HCl, 5ml HNO_3	Delineating	Swab or immerse from 30-60secs

3.3 Image Capturing

Microstructure observation and image capturing of the samples were performed using optical microscope (OM) equipped with open source software, AcQuis Image. Besides, imaging with scanning electron microscope (SEM) with secondary electron (SE) and backscattered electron (BSE) imaging was also performed. Energy dispersive spectroscopy (EDS) was conducted at selected areas of the samples [2].

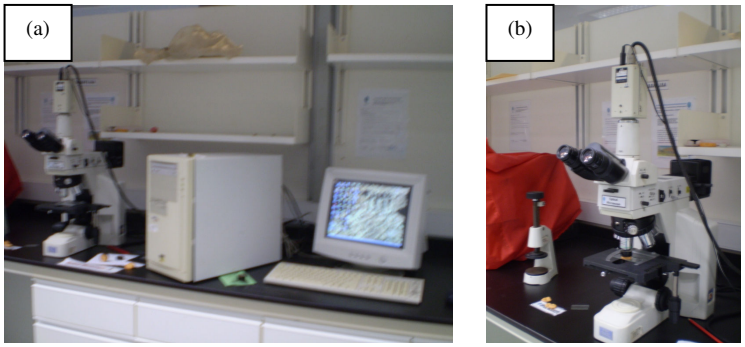

Figure 3.7: (a) Tools for image capturing, (b) Optical microscope (OM).

3.4 Data Analysis

Characterization and data analysis of the average particle size and particle area percentage of the primary carbides were measured using open source NIH ImageJ software. NIH ImageJ is a public domain Java image processing program inspired by NIH Image for the Macintosh. It runs, either as an online applet or as a downloadable application on any computer with a Java 1.4 or later virtual machine. Downloadable distributions are available for Windows, Mac OS, Mac OS X and Linux. It can display, edit, analyze, process, save and print 8-bit, 16-bit and 32-bit images. It can read many image formats including TIFF, GIF, JPEG, BMP, DICOM, FITS and "raw". It supports "stacks", a series of images that share a single window. It is multithreaded, so time-consuming operations such as image file reading can be performed in parallel with other operations. It can calculate area and pixel value statistics of user-defined selections. It can measure distances and angles. It can create density histograms and line profile plots. It supports standard image processing functions such as contrast manipulation, sharpening, smoothing, edge detection and median filtering. It does geometric transformations such as scaling, rotation and flips. The image can be zoomed up to 32:1 and down to 1:32. All analysis and processing functions are available at any magnification factor. The program supports any number of windows (images) simultaneously, limited only by available memory. Spatial calibration is available to provide real world dimensional measurements in units such as millimeters. Density or gray scale calibration is also available. NIH ImageJ was designed with an open

architecture that provides extensibility via Java plugins. Custom acquisition, analysis and processing plugins can be developed using NIH ImageJ's built in editor and Java compiler. User-written plugins make it possible to solve almost any image processing or analysis problem and the plugins code is freely available. In this project, NIH ImageJ was used to measure the average particle size and percentage area of each particle. This technique was chosen instead of the manual method specified by the ASTM standards because of its better accuracy and repeatability. In addition, the ASTM method is much slower and is rather difficult to perform [7].

NIH Image was developed at the Research Services Branch (RSB) of the National Institute of Mental Health (NIMH), a part of the National Institutes of Health (NIH). It reads and writes TIFF, PICT, PICS and MacPaint files. Therefore provides compatibility with various applications including programs for scanning, processing, editing, publishing and analyzing images. Image can be used to measure area, mean, centroid, perimeter, etc. of user defined regions of interest. It also performs automated particle analysis and provides tools for measuring path lengths and angles. Images are two dimensional arrays of pixels. An image requires one byte of RAM for each pixel plus a few thousand additional bytes for data structures containing information about the image, such as colour tables and calibration [10].

The next paragraphs illustrate the calculation of the average particle size and percentage area of Nb. All the methods described in these paragraphs are applied in the same manner to calculate the average particle size and percentage of Cr. Figure 3.8 shows the BSE image of the microstructure of the as-cast sample of O1 loaded by ImageJ. For ease in measuring the average particle size and percentage area of each particle, the image had to be cropped into small sections of images in order to not complicate the measuring process. Figure 3.9 shows the cropped image from the BSE image of the microstructure of the as-cast sample of O1 (Figure 3.8).

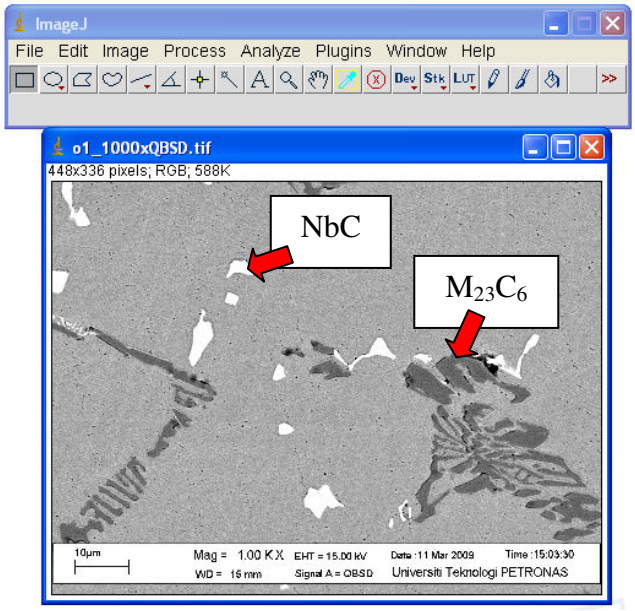

Figure 3.8: BSE image of the microstructure of the as-cast sample O1.

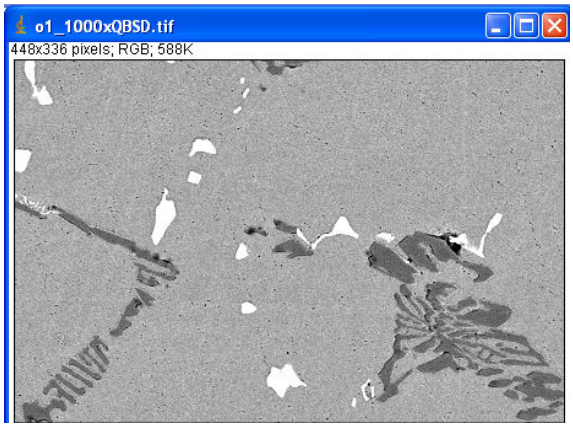

Figure 3.9: Cropped image from the BSE image of the microstructure of the as-cast sample O1.

After cropping, the image had to be enhanced or "thresholded" to invert the cropped image (Figure 3.9) into a red and white image as shown in Figure 3.10. To calculate the average particle size and percentage area of Nb, Figure 3.9 was threshold so that Nb

became red and Cr turned to white so that only Nb appeared in the pop out window (Figure 3.10). This was to ensure that only Nb was measured by NIH ImageJ.

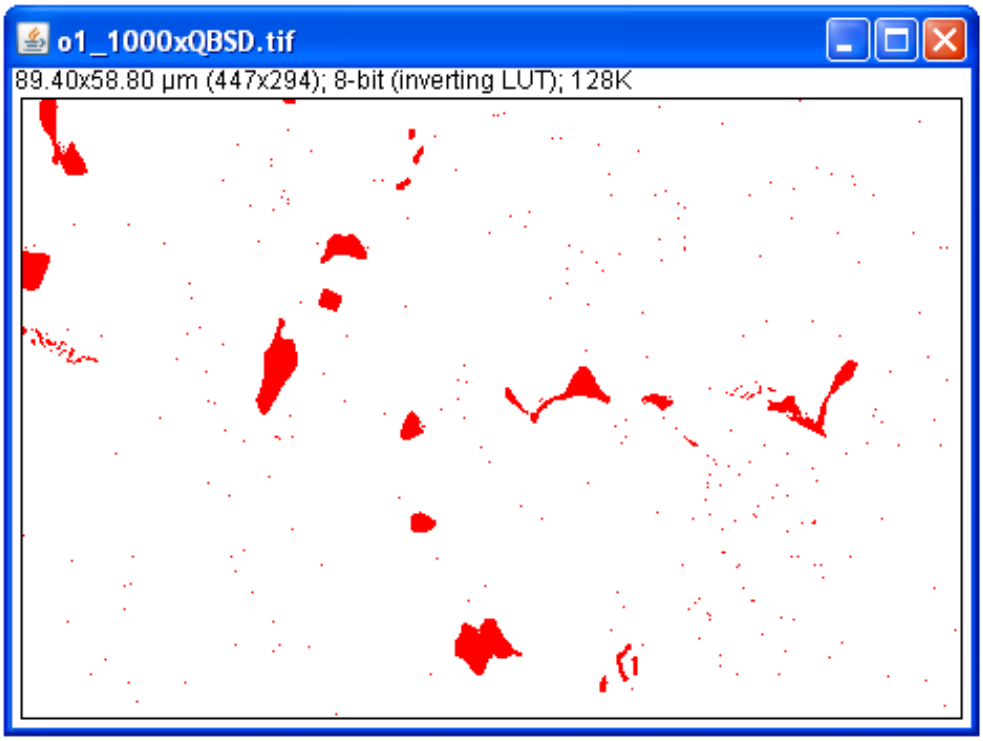

Figure 3.10: Threshold image of the cropped image from the BSE image of the microstructure of the as-cast sample O1.

After the image had been threshold, the Nb particle was analyzed. This command counts and measures the threshold image by scanning the selected particle until it finds the edges of the particle to complete an outline. The average particle size was measured based on the outline. Figure 3.11 shows the numbered outline of the particle, results and summary of the particle size. The results will then be tabulated in the spreadsheet.

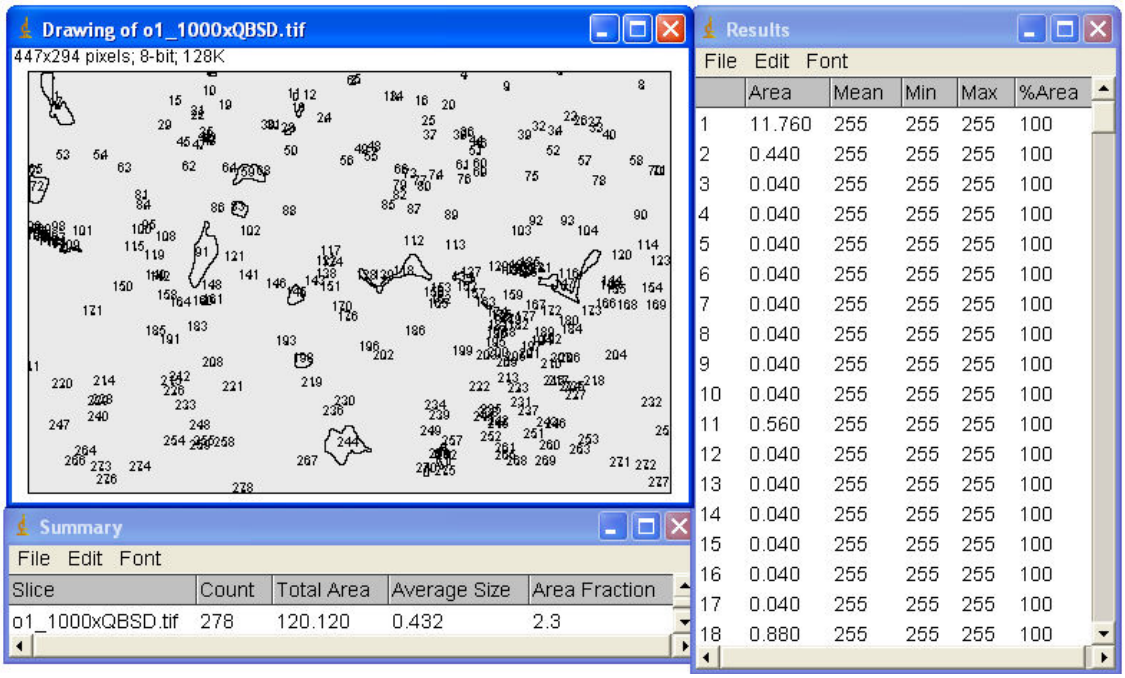

Figure 3.11: Outline numbered threshold image, results and summary of the results by the particle analyzer.

CHAPTER 4

RESULTS AND DISCUSSION

Figure 4.1 shows the microstructure of the as-cast material. The optical image (Figure 4.1a) shows the austenitic matrix (light coloured area) with a network of primary carbides (slightly darker area). There were no voids visible in the as-cast sample, O1.

The image obtained from the secondary electrons (Figure 4.1b) does not provide sufficient information about the types of carbides appeared in the material but the image obtained from the BSE image (Figure 4.1c), shows that the network is made of two different types of carbides which can be distinguished from the white and dark regions present in the image. The dark phase can be identified as Cr-rich $M_{23}C_6$, while the Nb-rich NbC phases appear as white regions due to the fact that Nb has greater atomic weight than Cr [3].

Energy Dispersive Spectroscopy (EDS) is performed on the grey, white, and dark regions. This is done to determine which region has the highest niobium or chromium concentration. The EDS analysis done in spot mode (Figure 4.2) indicates that the grey regions are rich in Cr, the white regions are rich in Nb, whereas the dark regions are rich in Ti.

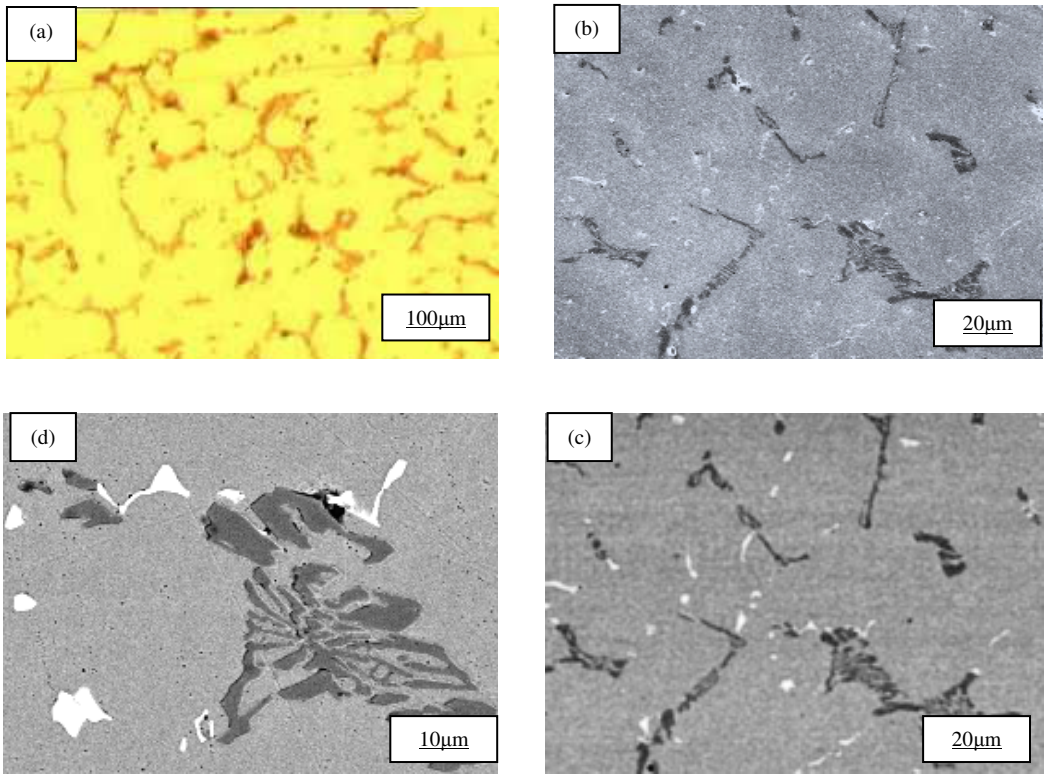

Figure 4.1: Microstructure of as-cast material, (a) optical microscope (OM) image of sample etched in glyceregia, (b) secondary electron (SE) image, (c) backscatter electron (BSE) image, (d) the fine and feathery shape of the microstructure in the as-cast sample.

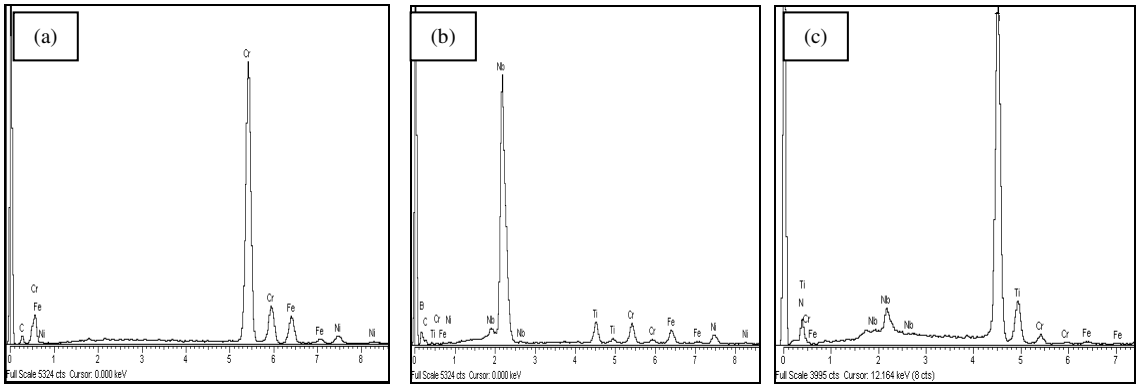

Figure 4.2: Spectra obtained by EDS in spot mode on the as-cast material, O1, (a) grey regions indicating Cr rich, (b) white regions indicating Nb rich, (c) dark regions indicating Ti rich.

Figure 4.3a shows the general appearance of the microstructure of the creep-tested sample, A1 under the optical microscope (OM) image, while Figure 4.3b shows the secondary electron microscope (SEM) image of the creep tested sample magnified to a specific microstructure from the creep-tested sample (Figure 4.3a) and Figure 4.3c is the backscatter electron (BSE) image of the magnified microstructure with the various types of precipitates labelled.

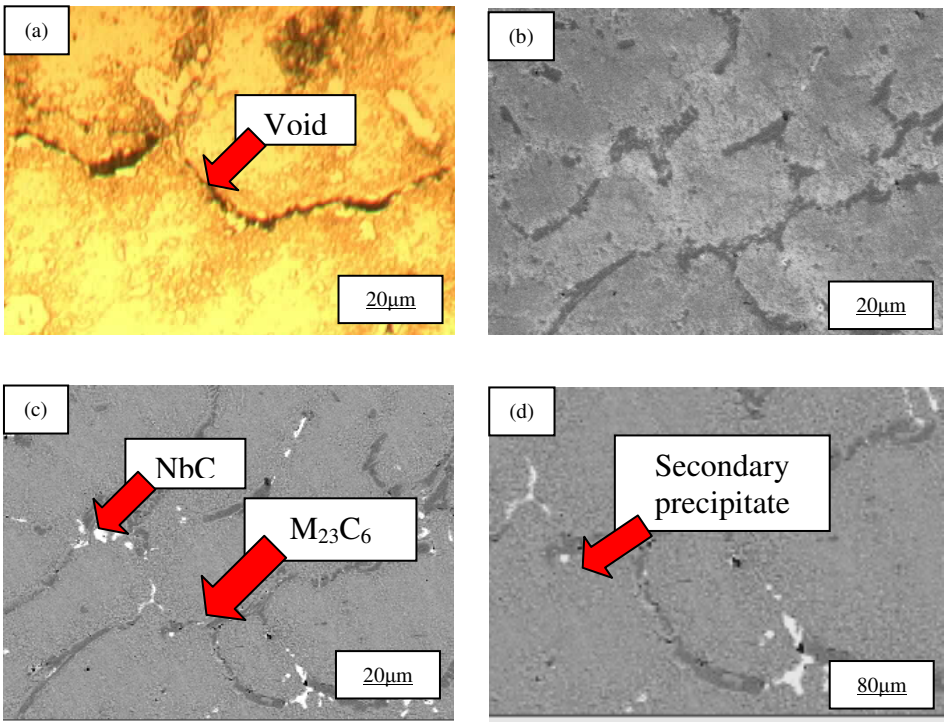

Figure 4.3: Microstructure of creep-tested material, A1, (a) optical microscope (OM) image of sample etched in glyceregia, (b) secondary electron (SE) image, (c) backscatter electron (BSE) image, (d) cropped image of backscatter electron (BSE) image identifying two precipitate types $M_{23}C_6$ and NbC.

Figure 4.4a shows the microstructure of the ex-service sample, K1 under the optical microscope (OM) image, while Figure 4.4b shows the secondary electron microscope (SEM) image magnified to a specific microstructure and Figure 4.4c is the backscatter

electron (BSE) image of the magnified microstructure with the various types of precipitates labelled.

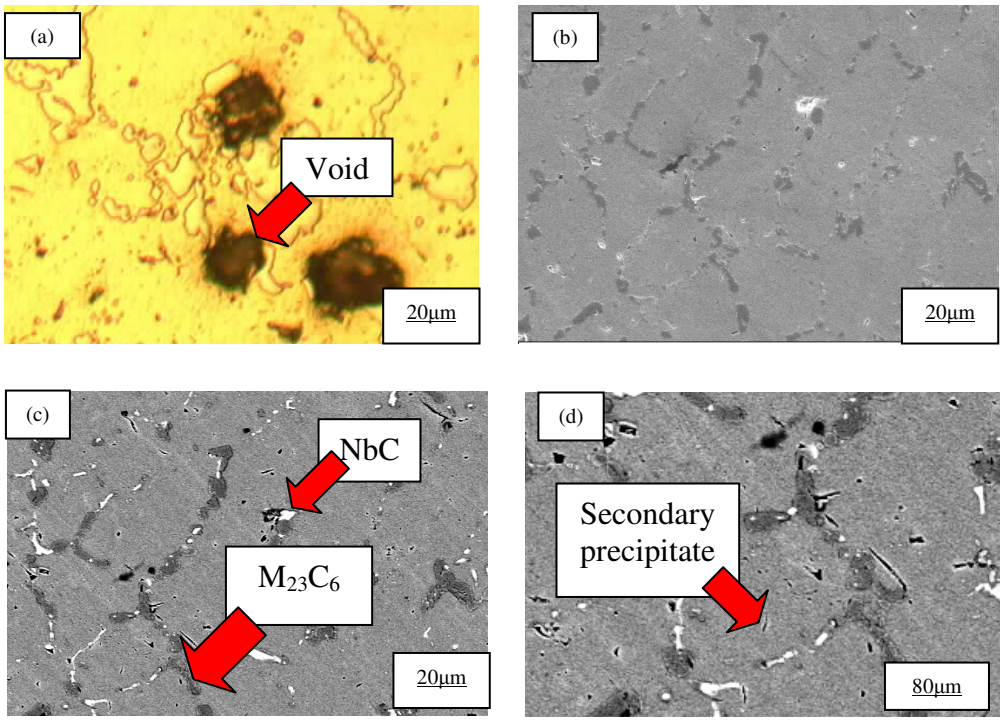

Figure 4.4: Microstructure of ex-service material, K1, (a) optical microscope (OM) image of sample etched in glyceregia, (b) secondary electron (SE) image, (c) backscatter electron (BSE) image, (d) cropped image of backscatter electron (BSE) image identifying two precipitate types $M_{23}C_6$ and NbC.

Identification of coarse precipitates was done by the backscatter electron (BSE) imaging and energy dispersive spectroscopy (EDS). There were two types of precipitates present in the material. The $M_{23}C_6$ Cr-rich appeared both intergranularly and as fine precipitation while NbC are found along the grain boundaries. TiC predominantly occurred intragranularly [1].

- $M_{23}C_6$: It is rich in Cr and it also has a combination of various types of metal and was presented as M_{23}.
- NbC: Nb-rich MC.

Distinctive comparison between the images from the as-cast (Figure 4.1), creep-tested samples (Figure 4.3), and ex-service samples (Figure 4.4) could be seen from the shape of the primary carbides present and the presence of additional microstructure in the form of small needle-like secondary carbides structures in the creep-tested samples (Figure 4.3c-d) and ex-service samples (Figure 4.4c-d). The shape of the primary carbides ($M_{23}C_6$ and NbC) in the ex-service sample is rounder (Figure 4.4c-d) compared to the creep-tested and finer shape (Figure 4.1c-d) of the as-cast sample.

One additional observation made on the creep-tested and ex-service samples were the presence of voids. The voids would appear as dark areas both in SE and BSE images (they also appear as dark areas in OM images). There were no voids detected in the as-cast sample (Figure 4.1a) and voids were observed in the creep-tested sample (Figure 4.3a) and ex-service sample (Figure 4.4a). To further study the pattern of the voids formed in the creep-tested samples, images were taken from the three samples, A1, A2, and A3.

Figure 4.5 shows the general appearance of the microstructure of the creep tested sample under the optical microscope (OM). The voids seemed to occur in groups or clustered together. The type of void identified is Type-W (Wedge). Figure 4.6 shows the microstructure of the ex-service material under optical microscope (OM). Voids are visible in the ex-service sample at the primary carbides area and scattered throughout the sample. The type of void identified is Type-R (Round) [2].

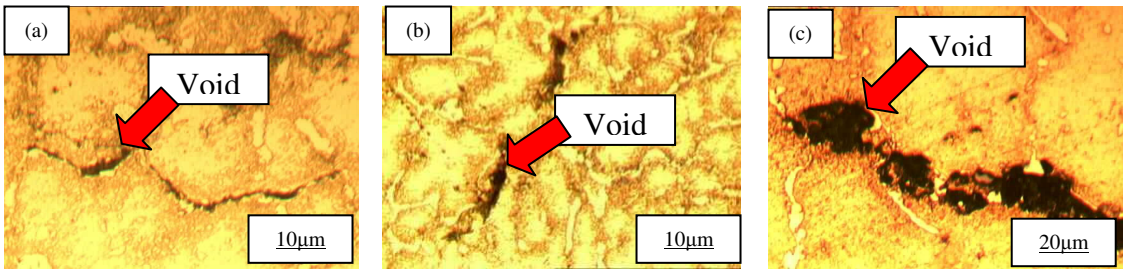

Figure 4.5: Microstructure of creep-tested material via OM showing voids, (a) sample A1, (b) sample A2, (c) sample A3.

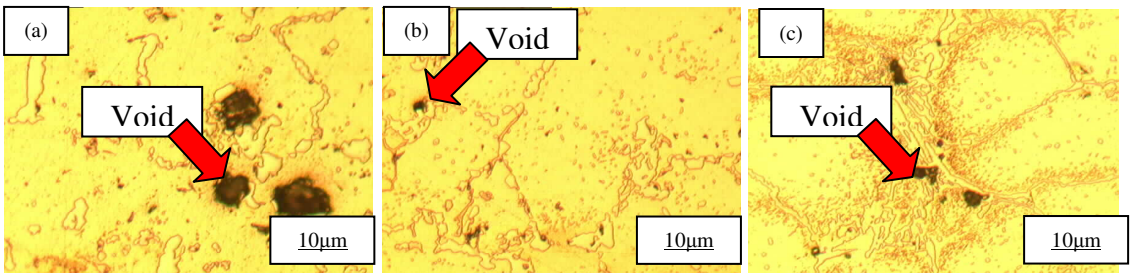

Figure 4.6: Microstructure of ex-service material via OM showing voids, (a) sample K1, (b) sample K2, (c) sample K3.

Table 4.1 shows the average particle size and the percentage area measured by using NIH ImageJ and then compared with intercept method as in the ASTM standards. As-cast sample O1 had been chosen randomly to be measured. It was to make sure that the average particle size and the percentage area obtained from NIH ImageJ were accurate as obtained by the ASTM Intercept method. From Table 4.1, the error difference between the two methods was only about 2. Therefore it is proved that NIH ImageJ is as reliable as the ASTM Intercept method (see Appendix A) in obtaining the average particle size and the percentage area as it is easier and faster to obtain values when compared to the ASTM Intercept method.

Table 4.1: Average particle size and percentage area of as-cast sample O1 measured using the NIH ImageJ and ASTM Intercept method.

Sample	**Average Particle Size (µm²)**		**Percentage Area (%)**	
	Chromium	**Niobium**	**Chromium**	**Niobium**
NIH ImageJ	49	11	5	2
ASTM Intercept Method	50.8	11.5	6.2	2.9
Error Difference	1.8	0.5	1.2	0.9

The average particle size and percentage area of the primary carbides present in the as-cast sample O1, creep-tested samples of A1, A2, and A3, and ex-service sample of K1, K2, and K3 were measured by NIH ImageJ were shown in Table 4.2 and Figure 4.7. From the result obtained, the average particle size and percentage area increases as the temperature increases.

Table 4.2: Average particle size and percentage area of samples measured using the NIH ImageJ.

Sample	Average Particle Size (μm²)		Percentage Area (%)	
	Chromium	Niobium	Chromium	Niobium
O1	49	11	5	2
A1	59	10	10	6
A2	58	9	10	5
A3	51	7	10	3
K1	51	37	12	11
K2	44	25	7	4
K3	25	18	5	3

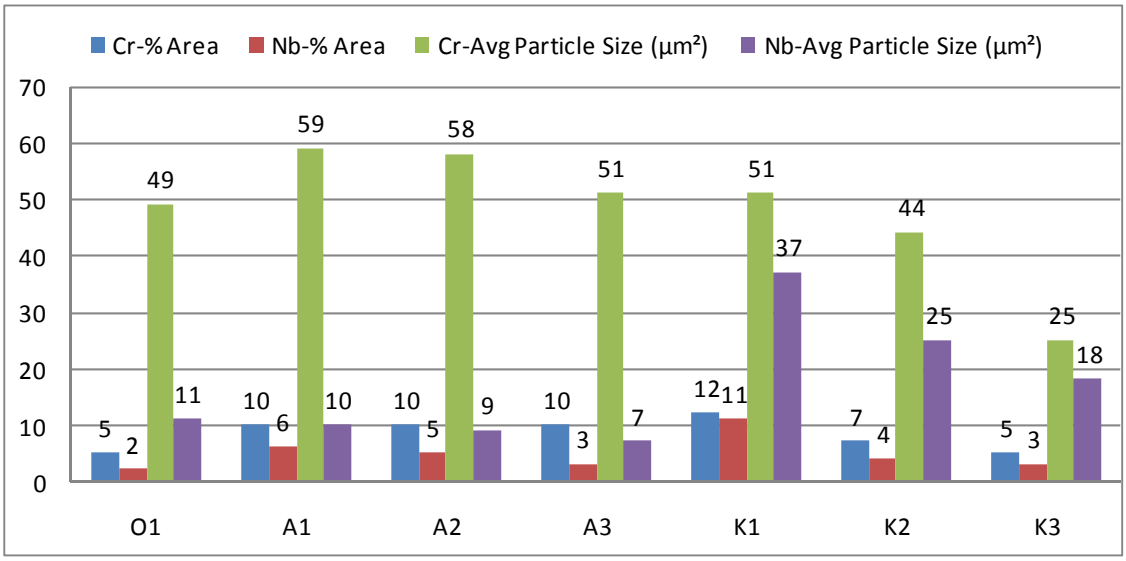

Figure 4.7: Average particle size and percentage area of Cr and Nb in the samples by NIH ImageJ.

CHAPTER 5

CONCLUSION AND RECOMMENDATION

The effect of creep could be seen by comparing the transformation of the microstructure in the creep-tested samples with the as-cast sample. It was found that the microstructure in the as-cast samples consisted of an austenitic matrix and a network of two types of primary carbides (chromium and niobium), whereas that of the creep tested materials in addition by having the primary carbides also exhibit a fine dispersion of small needle-like structure, decomposition of primary carbides into secondary carbides was found to occur as creep progressed. Exposure at the service temperature may promote the dissolution of primary carbides and development of a fine array of secondary carbides precipitated from the highly supersaturated matrix [11].

In this project, the average particle size and percentage area of $M_{23}C_6$ and NbC carbides for the creep-tested samples and ex-service decreases as temperature decreases. The reduction of $M_{23}C_6$ average particle size and percentage area is believed to be due to Cr being dissolved into the matrix to form secondary $M_{23}C_6$ precipitates [11]. On the other hand, the significant decrease in average particle size and percentage area of NbC is believed to be due to formation of other precipitates such as titanium carbide, TiC (see Appendix C). This was proved from previous work done by Moon et al [8].

The shape of the primary carbides ($M_{23}C_6$ and NbC) in the ex-service sample is rounder compared to the creep-tested and finer shape of the as-cast sample with increasing service time and temperature. It is because of with increasing service time and temperature, the primary carbides tend to coarsen into rounder precipitates [1]. The author belief the increase in size for the primary carbides is simply the result of smaller islands of precipitate joining together. For $M_{23}C_6$, the average particle size increases by stealing the Cr from the regions around it.

For this material, Nb and Ti are added to stabilize the matrix and precipitates. Normally, without Nb and Ti, the regions around $M_{23}C_6$ will be depleted of Cr as $M_{23}C_6$ particle size increases by taking the Cr from the vicinity. Corrosion and other issues will become worse at the regions where Cr is depleted. Nb and Ti help to reduce this by discouraging the $M_{23}C_6$ to form in the vicinity.

There are no creep voids detected in the as-cast sample but voids seemed to form in the creep-tested samples and ex-service samples. As time and service temperature increasing, stress pulled apart the microstructure to form creep voids. The creep voids seemed to occur in groups or clustered together forming a line at boundaries between two grains. The type of creep voids in ex-service sample is Type-R (round), whereas in creep-tested sample is Type-W (wedge) [2]. A possible explanation would be that creep voids are most likely to nucleate at the grain boundaries because of vacancies due to lattice mismatch between carbide and austenite [1].

The main lessons gained and learned through this project was how to do metallographic sample preparation techniques, and to use various microstructure characterization techniques and tools to study material behaviour. This project also gave an insight about the creep phenomena and effect of creep to the transformation of the microstructure as creep progressed through the whole life period of the reformer tubes. This project is beneficial as it gave an understanding of how creep progressed and its effect on the reformer tube material. This would also present an opportunity for the manufacturers to further improve the metallurgy of the material so that the life of the reformer tube could

be extended. It would also provide vital information on evaluating the performance of Cr and Nb additions in creep strengthening mechanism. This project also gave a review of how microstructure characterization could be done [7].

For future work recommendation, the ex-service samples could be study in term of different location on the reformer tube, between inner wall and outer wall so that the transformation of the microstructure could be studied further as per location, as the samples were only small representative of what the actual creep progression really occur during steam-methane reforming process.

REFERENCES

[1] Abdul Wahab A., Kral M.V., 3D Analysis of Creep Voids in Hydrogen Reformer Tubes, Materials Science and Engineering A 412 (2005) 222-229.

[2] Abdul Wahab A., Private communication, Universiti Teknologi PETRONAS, Malaysia, 2008.

[3] Almeida L.H., Iain L.M., Ribeiro A.F., Microstructural Characterization of Modified 25Cr-35Ni Centrifugally Cast Steel Furnace Tubes, Material Characterization 49 (2003) 219-229.

[4] Brown, LeMay, Bursten, Chemistry the Central Science, New York, 2003.

[5] Crabtree G.W., Dresselhaus M.S., Buchanan M.V., The Hydrogen Economy, Physics Today, 2004.

[6] HARVEST ENERGY TECHNOLOGY, http://www.harvest-echnology.com/.

[7] Ismail M.A., Microstructure Characterization of Creep-tested Reformer Tube Material, Universiti Teknologi PETRONAS, Malaysia, 2008.

[8] Moon J., Kim S., Jeong H., Lee J., Lee C., Influence of Nb Addition on the Particle Coarsening and Microstructure Evolution in a Ti-Containing Steel Weld HAZ, Materials Science and Engineering A 454-455 (2007) 648-653.

[9] PROCESS ENGINEERING FOR PLANT, http://comtecquest.com.

[10] Research Services Branch, http://rsb.info.nih.gov/ij/.

[11] Rodriguez J., Haro S., Velaso A., Colas R., A Metallographic Study of Aging in a Cast Heat Resisting Alloy, Material Characterization 45 (2000) 25-32.

[12] Schmidt+Clemens, G/CA 4852 Micro Material Data Sheet, 2001.

[13] Turner S., Creep of Polymeric Materials, Encyclopedia of Materials: Science and Technology, Oxford: Elsevier Science Ltd. (2001) 1813-1817. ISBN 0-08-043152-6.

[14] Worden S., Microstructural Analysis of Creep Damage in Methanol Reformer Tubes, University of Canterbury, New Zealand, 2000.

APPENDIX A
USING NIH IMAGEJ

NIH IMAGEJ

Measuring Nb particle size and percentage area using NIH ImageJ:

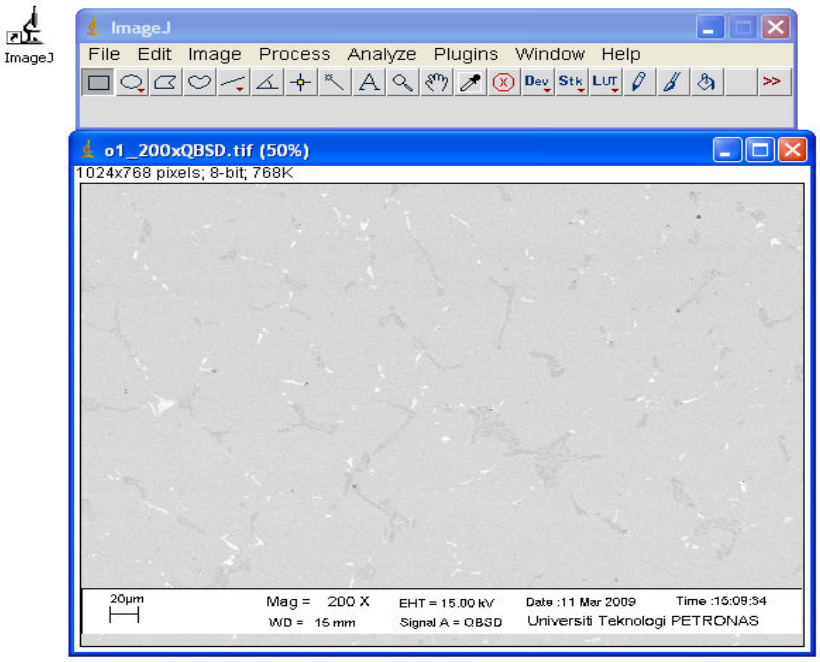

Figure A-1: BSE image of as-cast sample of O1 loaded by NIH ImageJ.

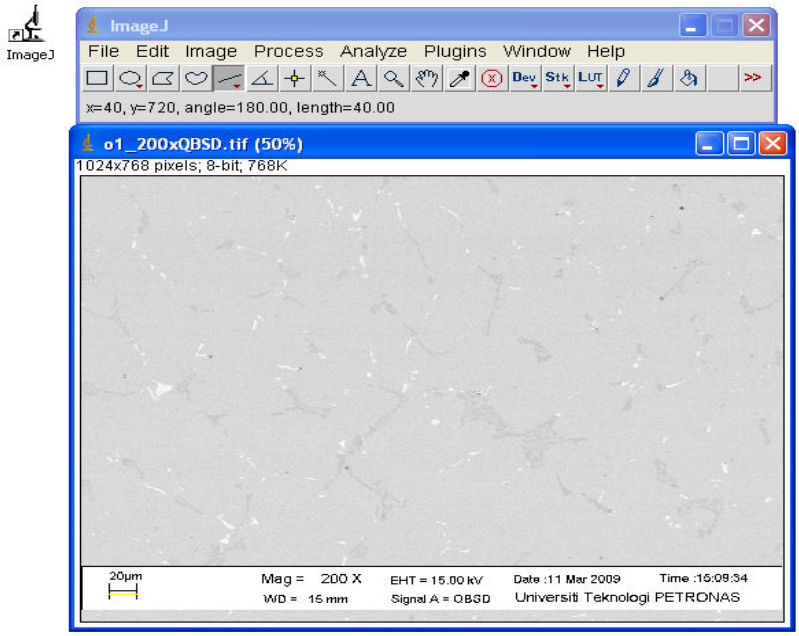

Figure A-2: Measuring length of scale (bottom left corner).

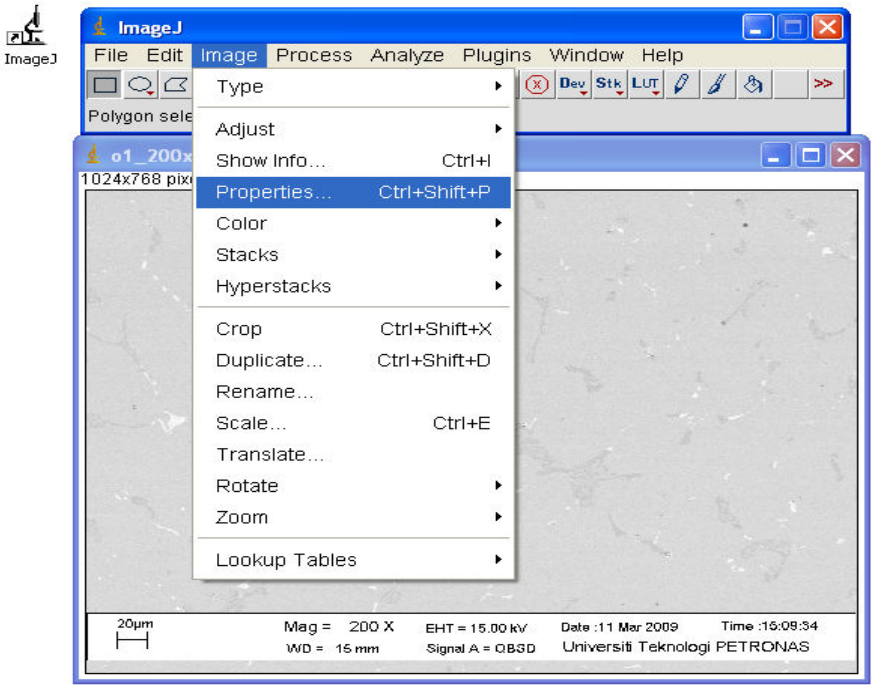

Figure A-3: Clicking at "Image" toolbar > "Properties" toolbar.

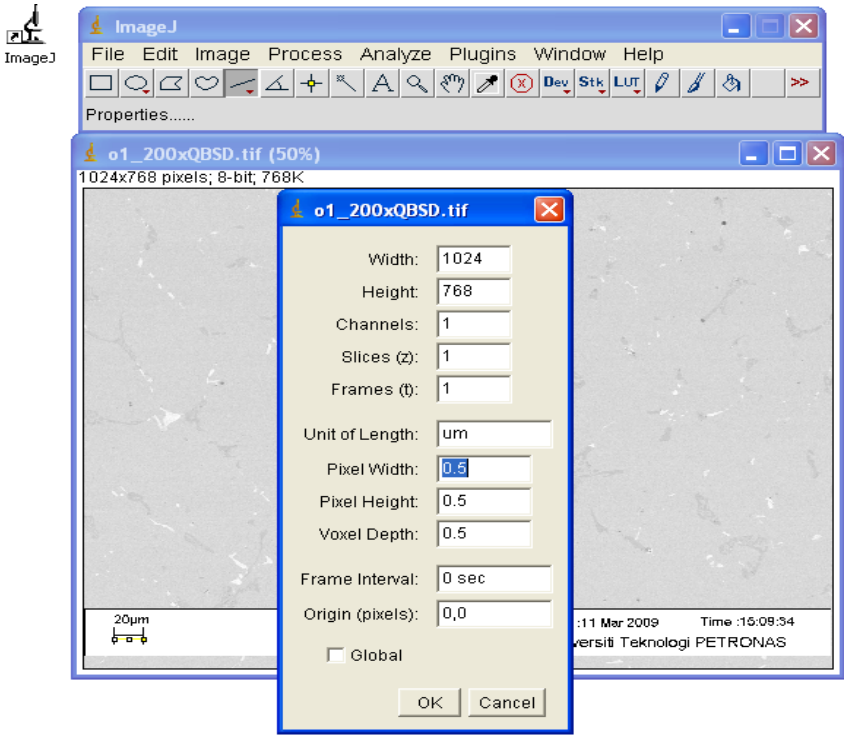

Figure A-4: Converting from pixel to unit of length and inputting the conversion factor.

Unit of length = µm
Pixel width = scale / length of scale
= 20 / 40
= 0.5

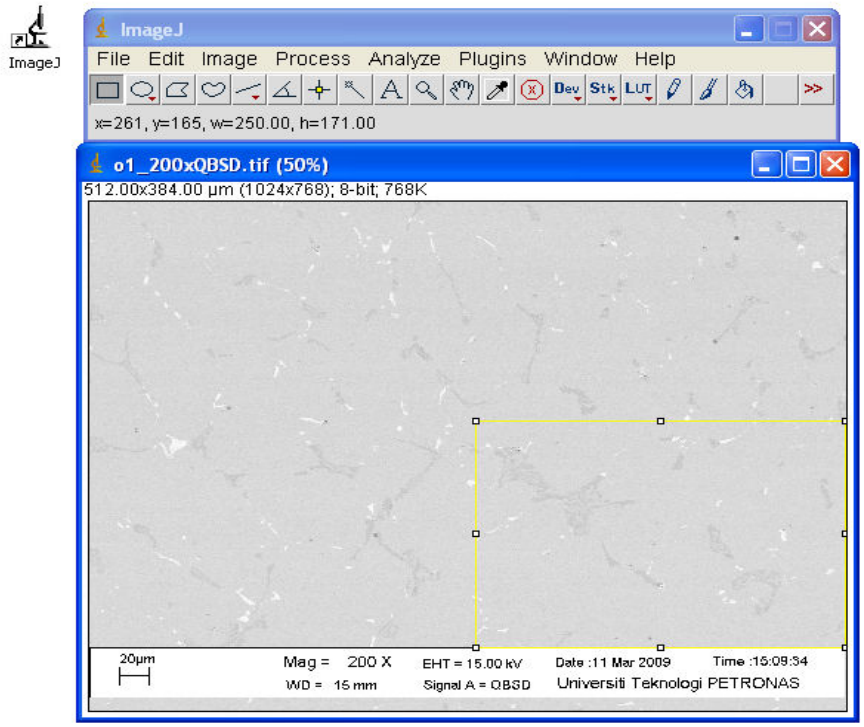

Figure A-5: Cropping a portion of the BSE image.

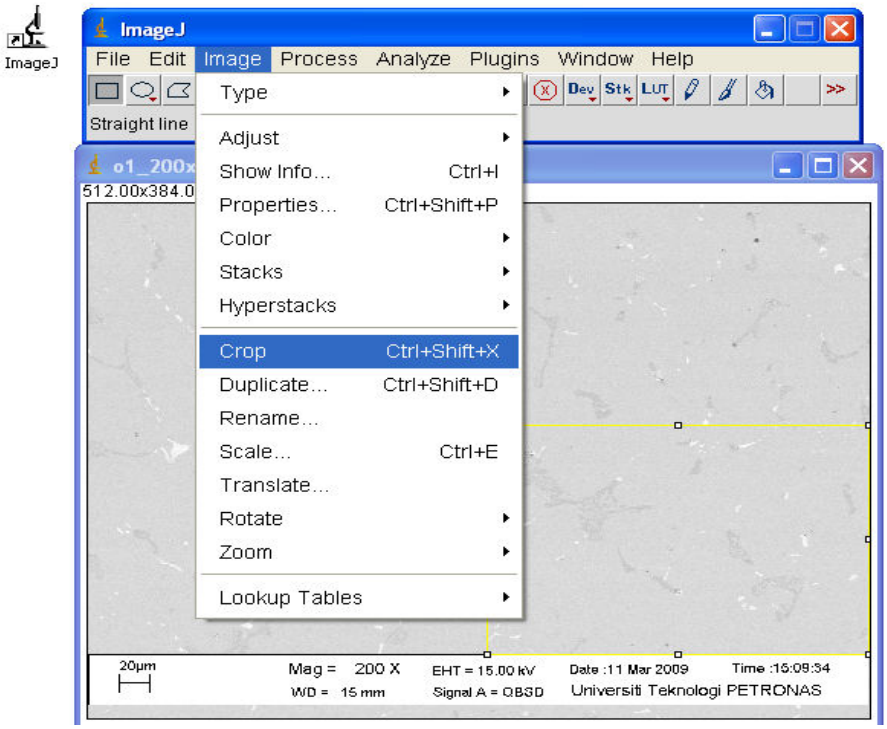

Figure A-6: Clicking at “Image” toolbar > “Crop” toolbar.

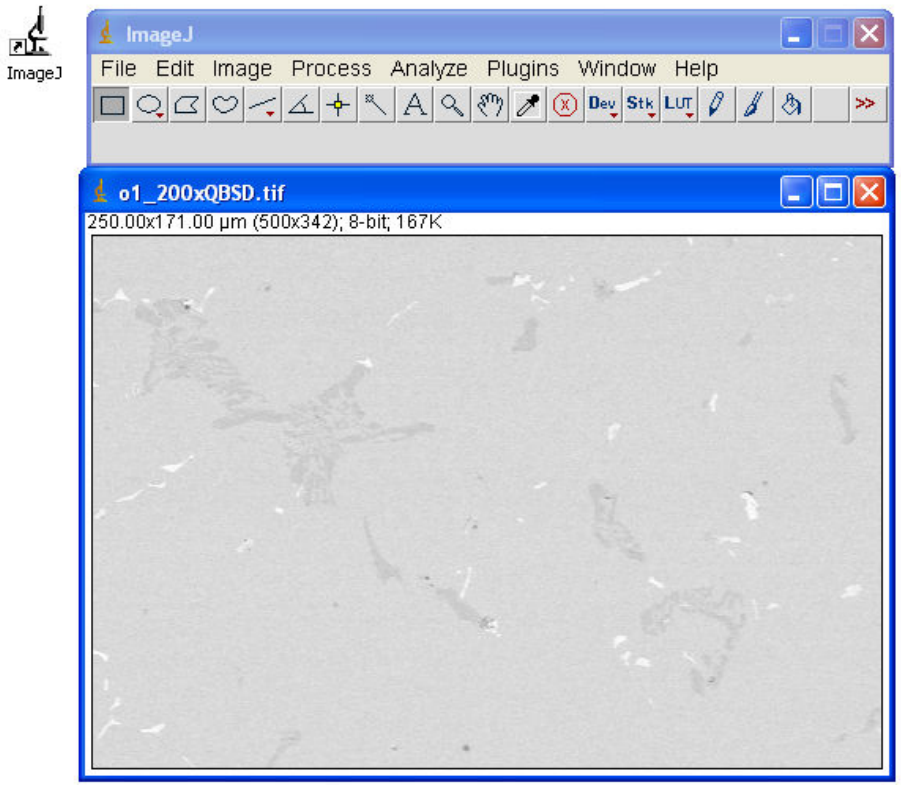

Figure A-7: Cropped BSE image to measure Nb.

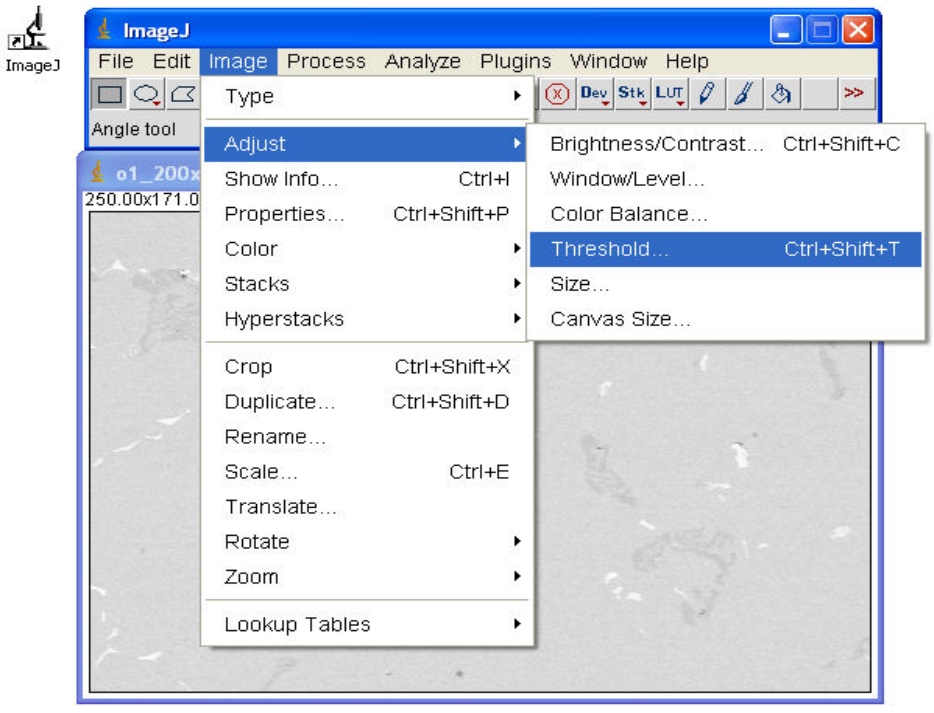

Figure A-8: Clicking at “Image” toolbar > “Adjust” toolbar > “Threshold” toolbar.

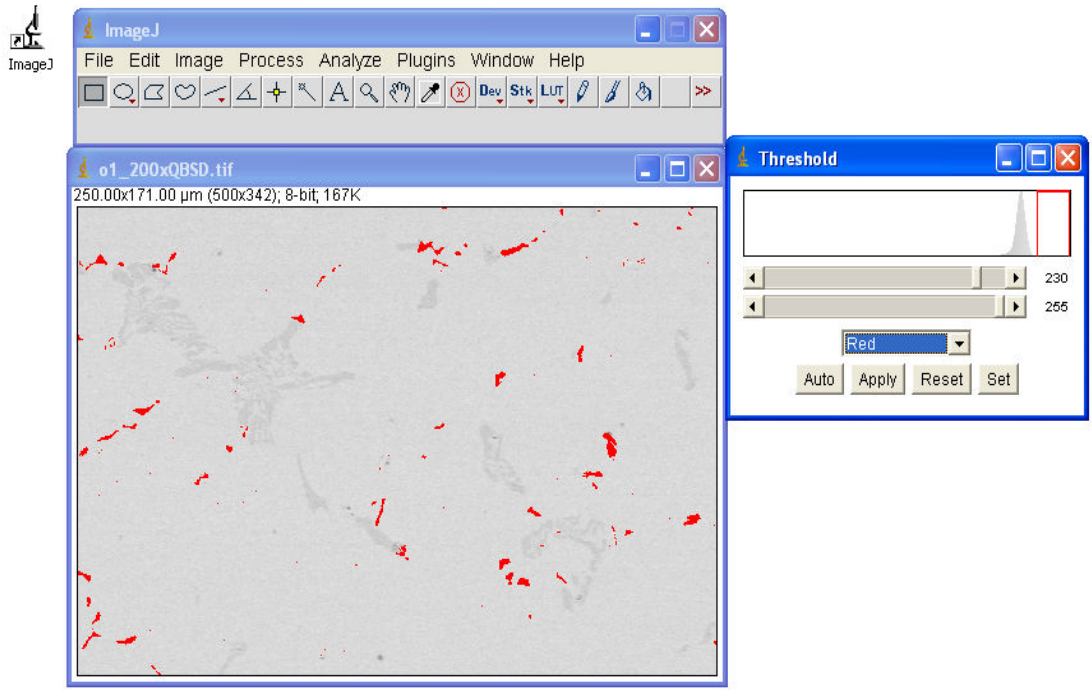

Figure A-9: Adjusting the red and white mode of “Threshold” limits to show only Nb.

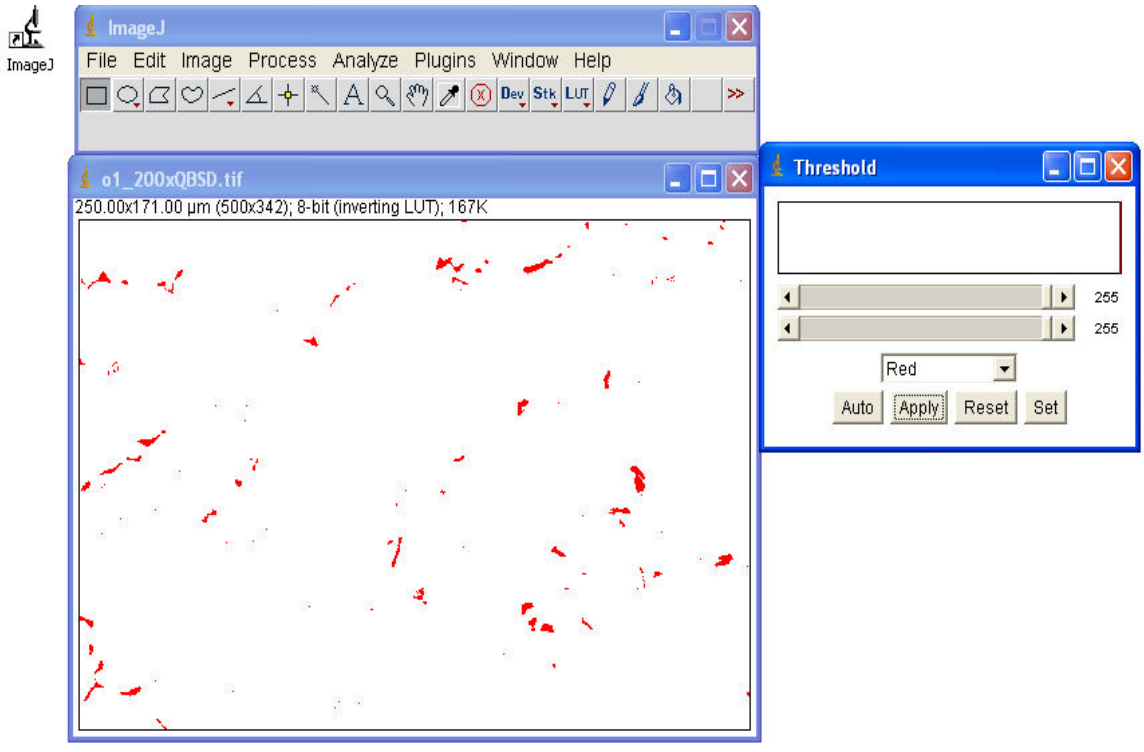

Figure A-10: Nb image (red) only appeared at pop out window.

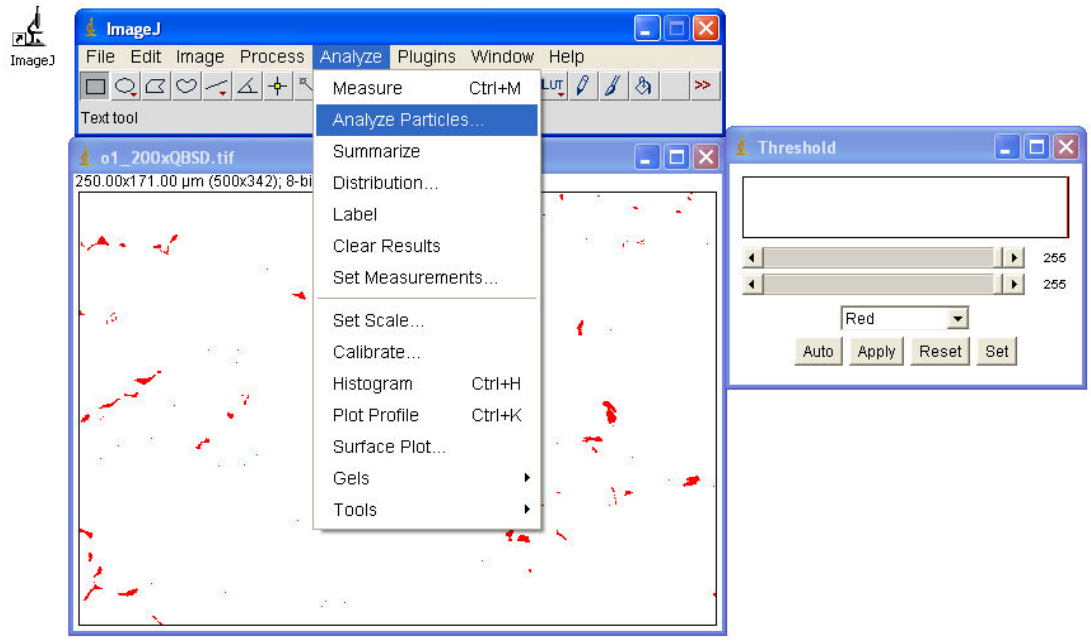

Figure A-11: Clicking at “Analyze” toolbar > “Analyze Particle” toolbar.

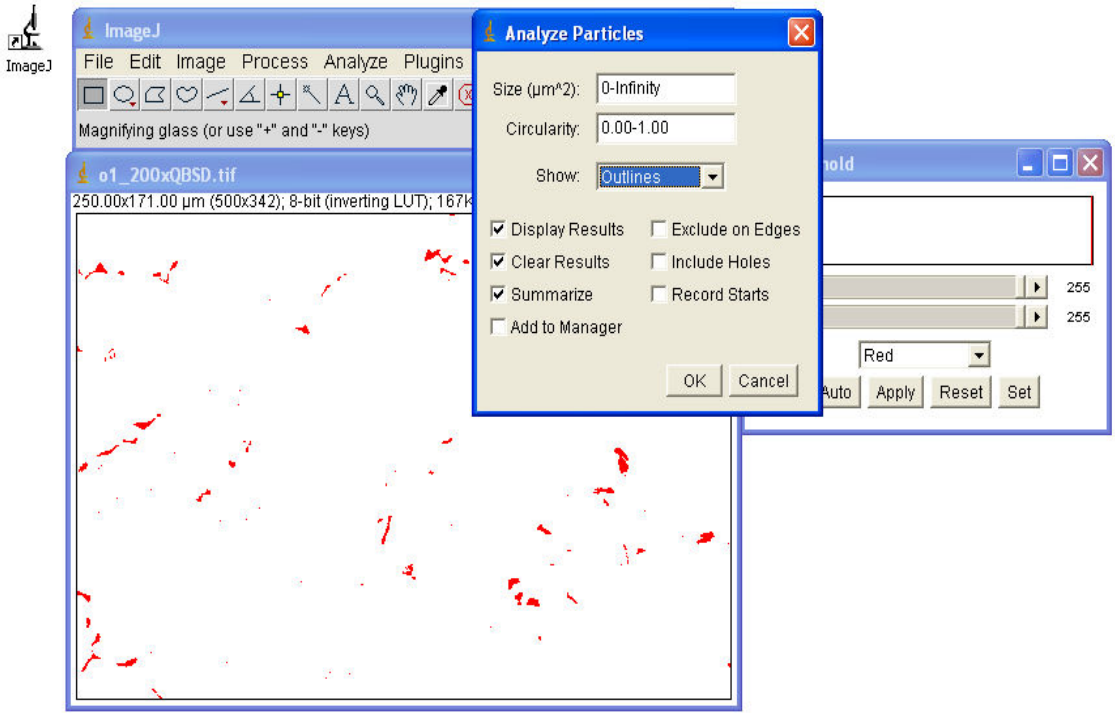

Figure A-12: Changing the “Show” input box from “Nothing” to “Outlines”.

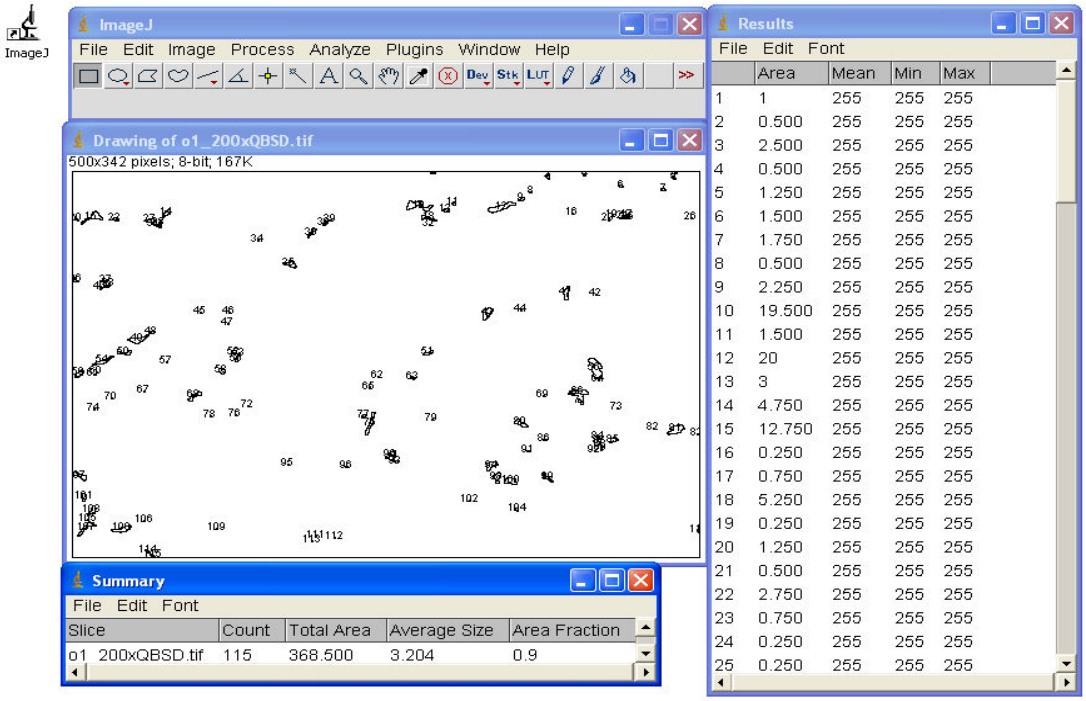

Figure A-13: Result, summary and outline numbered of the cropped Nb image.

Measuring Cr particle size and percentage area using NIH ImageJ:

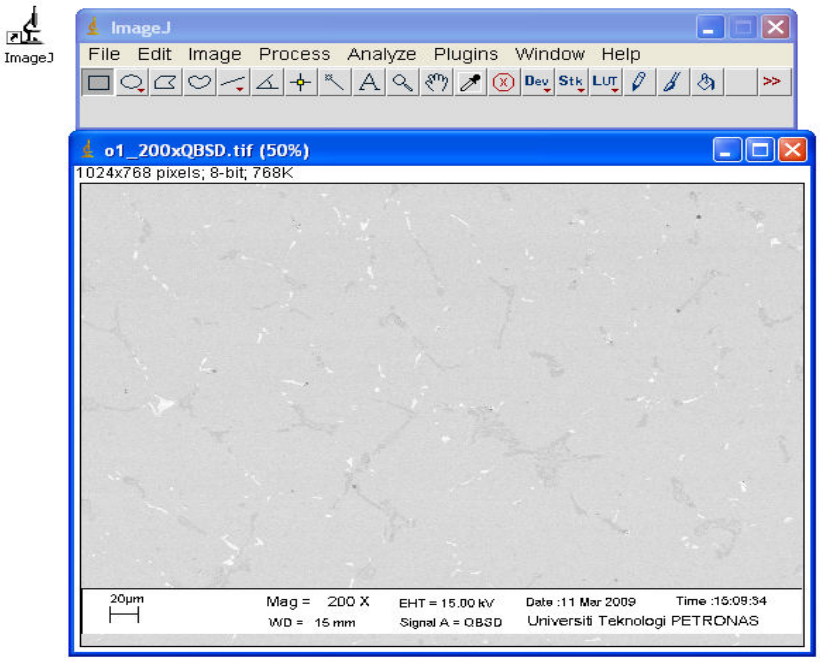

Figure A-14: BSE image of as-cast sample of O1 loaded by NIH ImageJ.

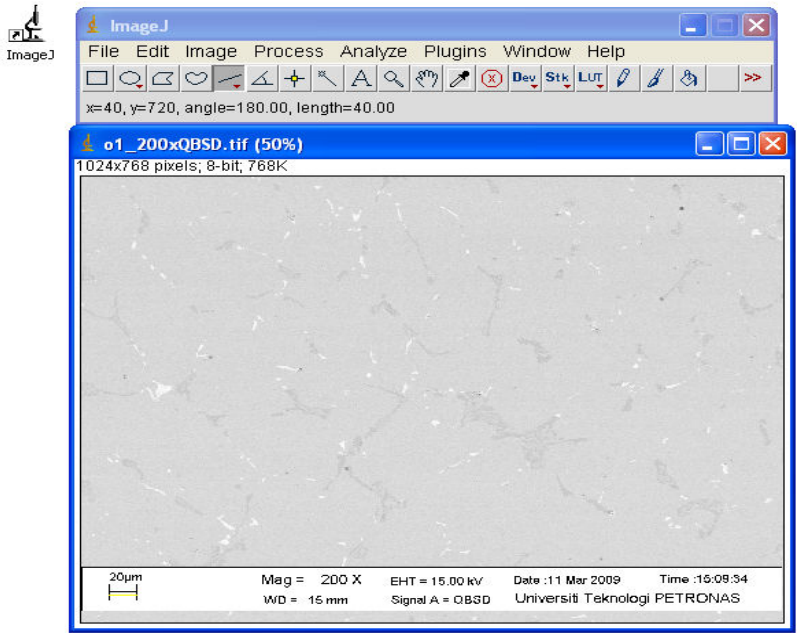

Figure A-15: Measuring length of scale (bottom left corner).

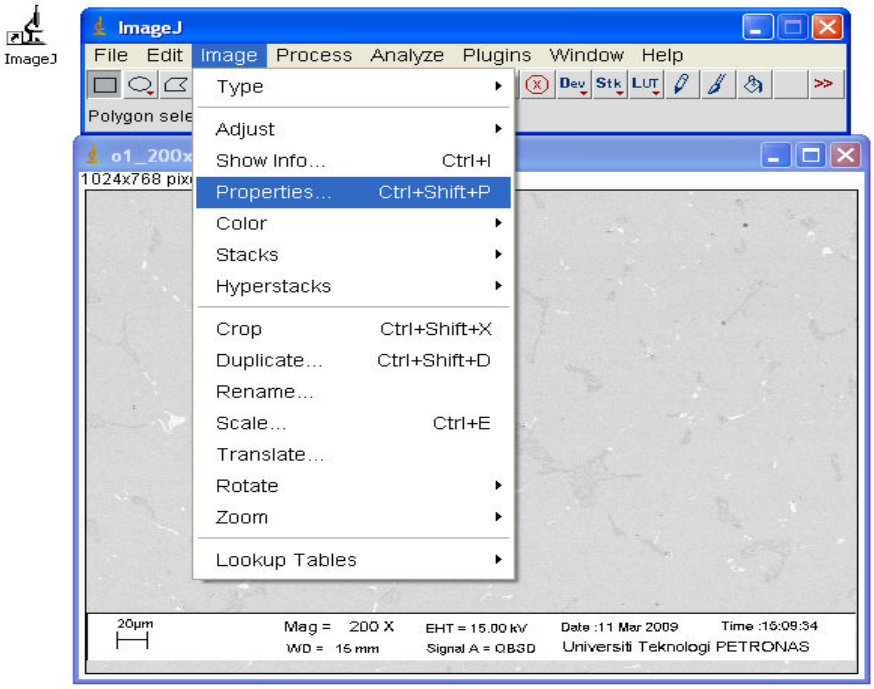

Figure A-16: Clicking at "Image" toolbar > "Properties" toolbar.

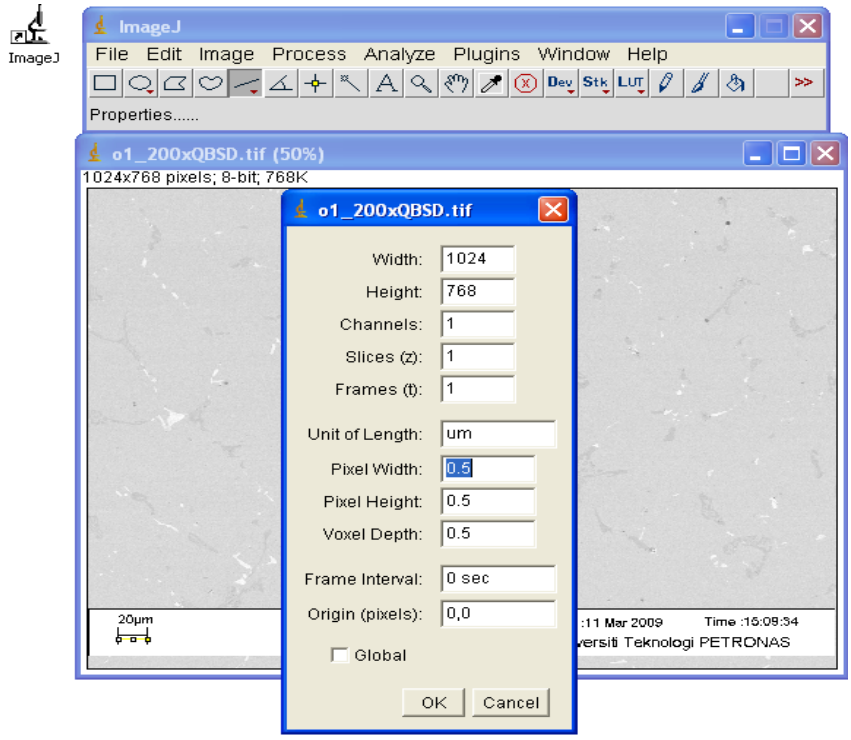

Figure A-17: Converting from pixel to unit of length and inputting the conversion factor

Unit of length = µm
Pixel width = scale / length of scale
= 20 / 40
= 0.5

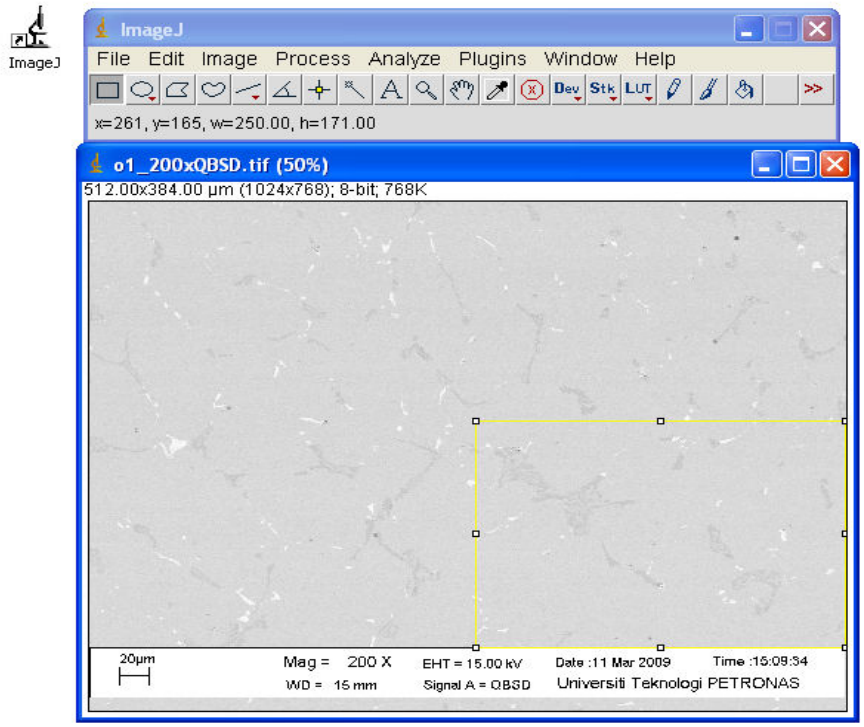

Figure A-18: Cropping a portion of the BSE image.

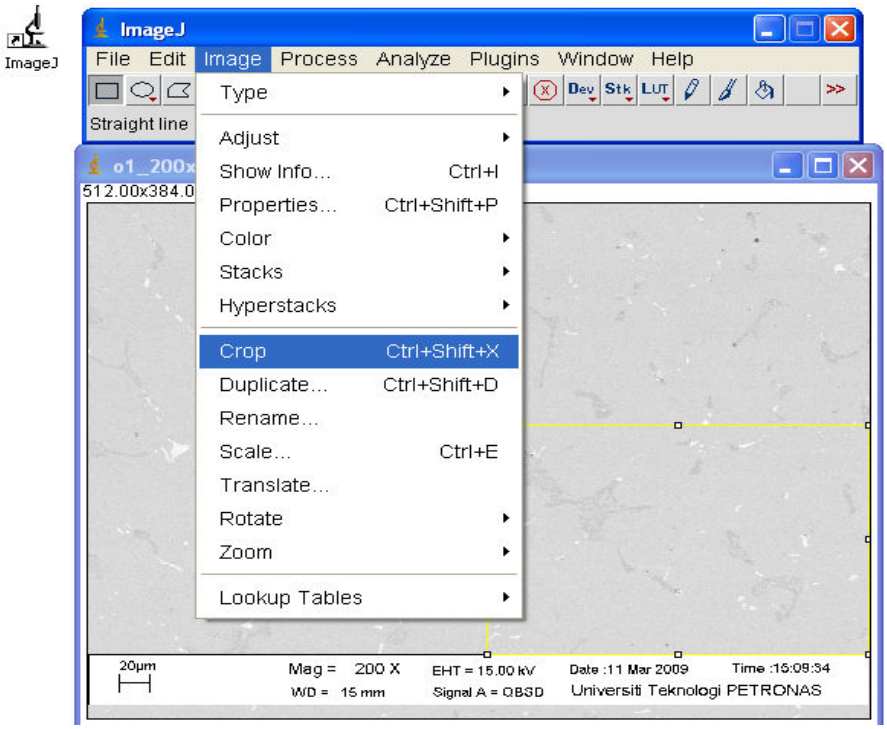

Figure A-19: Clicking at “Image” toolbar > “Crop” toolbar.

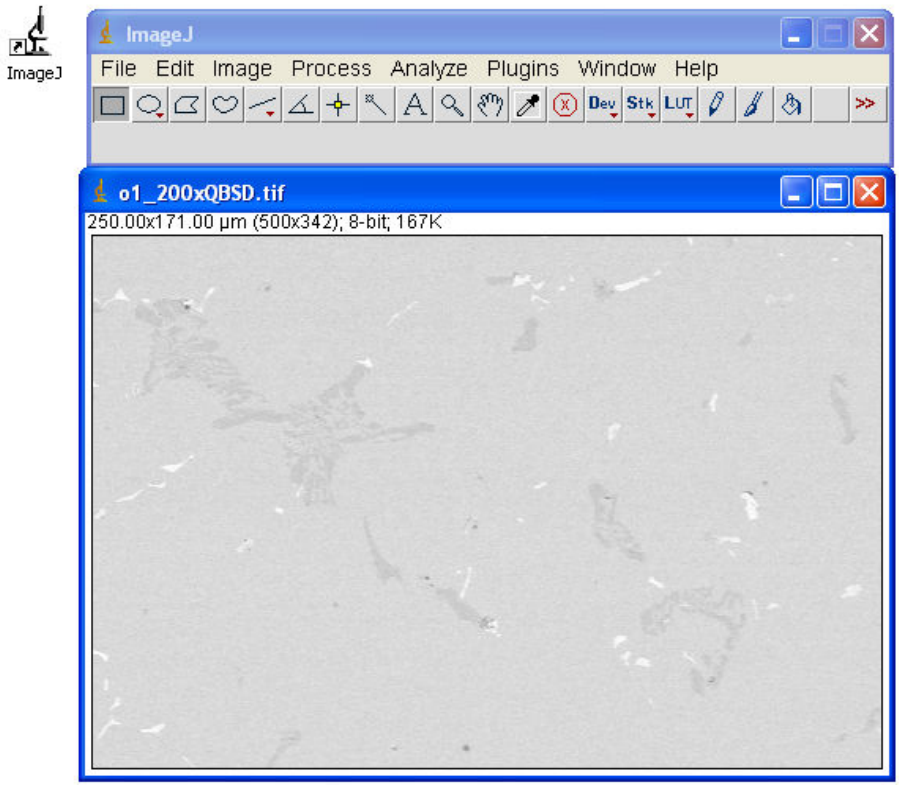

Figure A-20: Cropped BSE image to measure Cr.

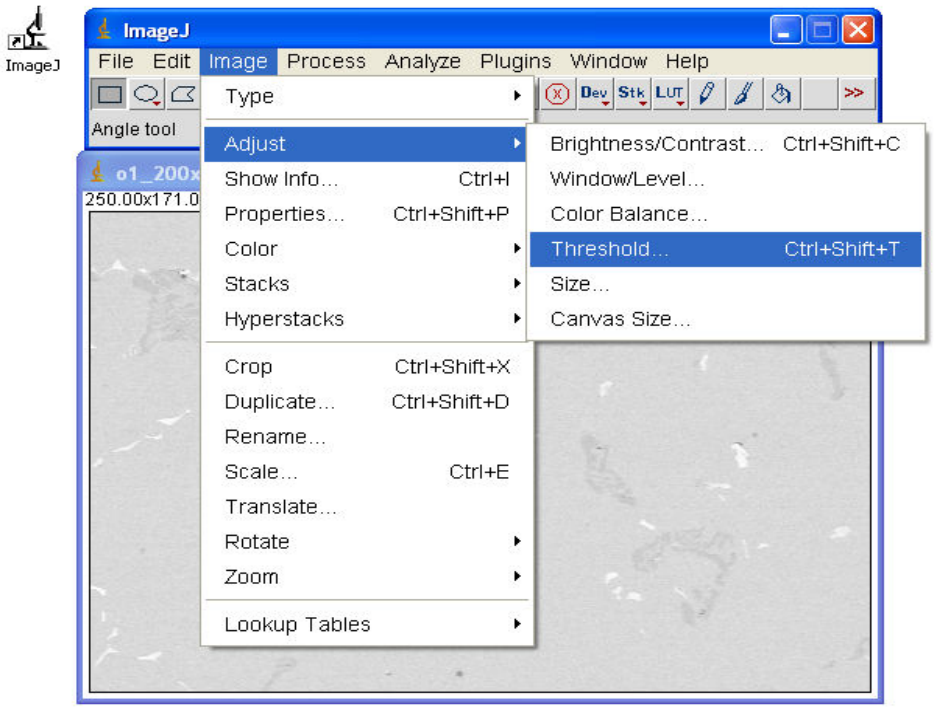

Figure A-21: Clicking at “Image” toolbar > “Adjust” toolbar > “Threshold” toolbar.

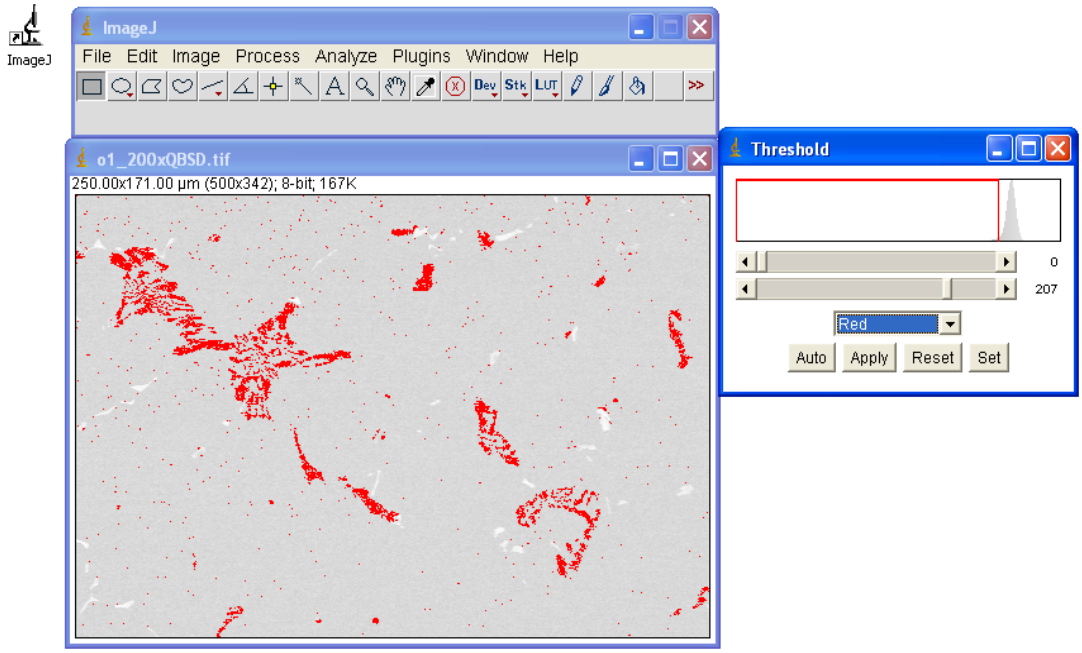

Figure A-22: Adjusting the red and white mode of “Threshold” limits to show only Cr.

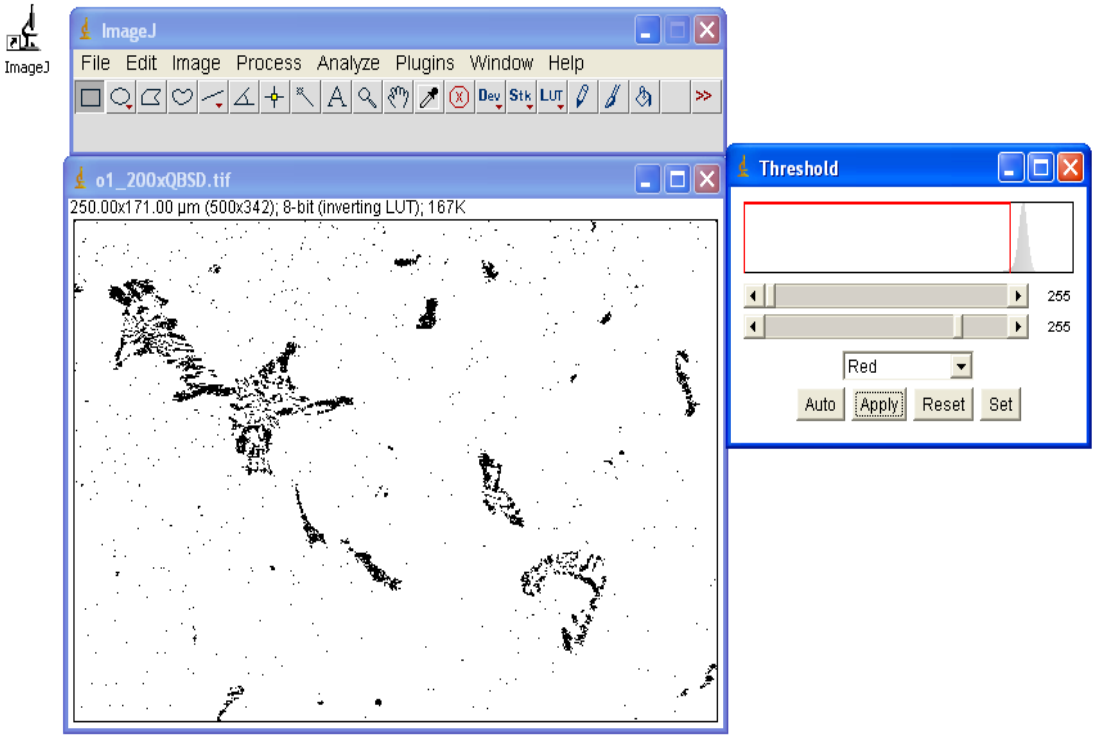

Figure A-23: Cr image (black) only appeared at pop out window.

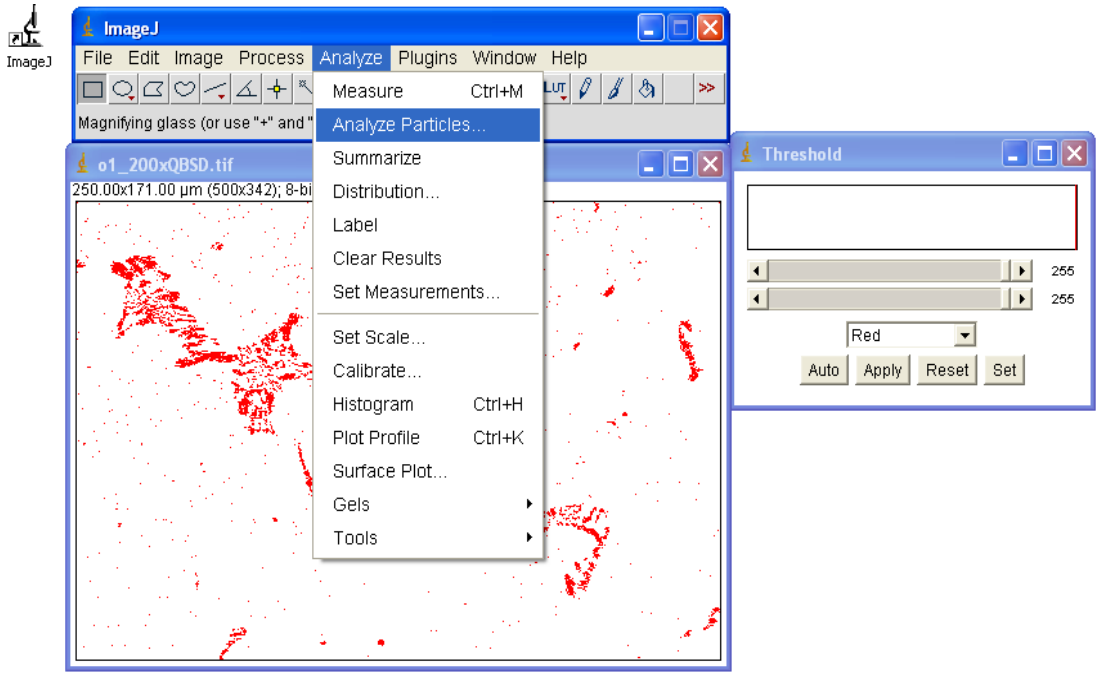

Figure A-24: Clicking at “Analyze” toolbar > “Analyze Particle” toolbar.

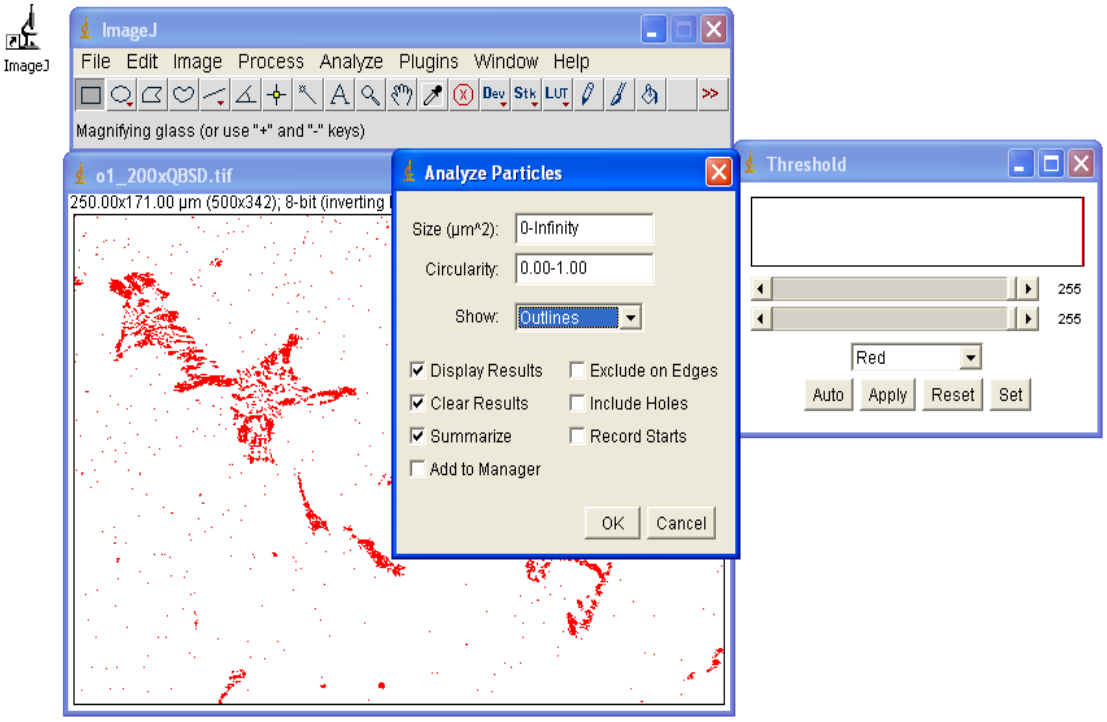

Figure A-25: Changing the “Show” input box from “Nothing” to “Outlines”.

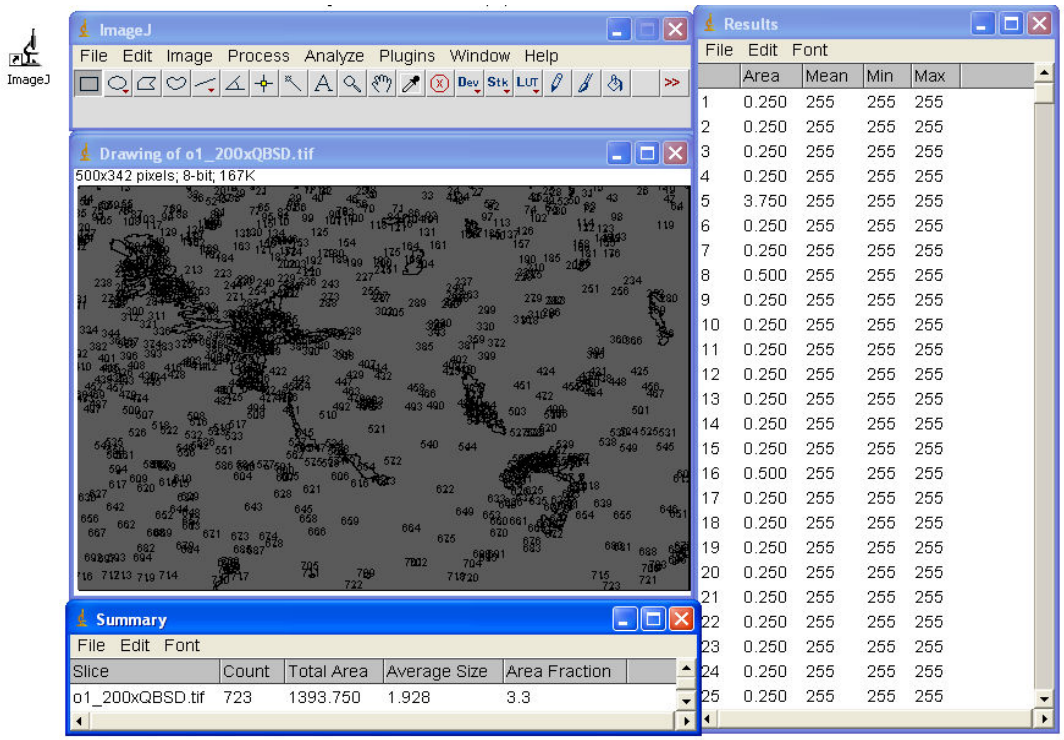

Figure A-26: Result, summary and outline numbered of the cropped Cr image.

APPENDIX B
RESULTS

Table B-1: Average particle size and percentage area of the samples using NIH ImageJ.

Sample	Count		Total Area (µm)	Average Particle Size (µm)		Percentage Area (%)	
	Cr	Nb		Cr	Nb	Cr	Nb
01	170	305	11799	49	11	5	2
A1	217	438	27409	59	10	10	6
A2	233	1365	25537	58	9	10	5
A3	334	695	21857	51	7	10	3
K1	394	513	39182	51	37	12	11
K2	320	200	18935	44	25	7	4
K3	259	401	13611	25	18	5	3

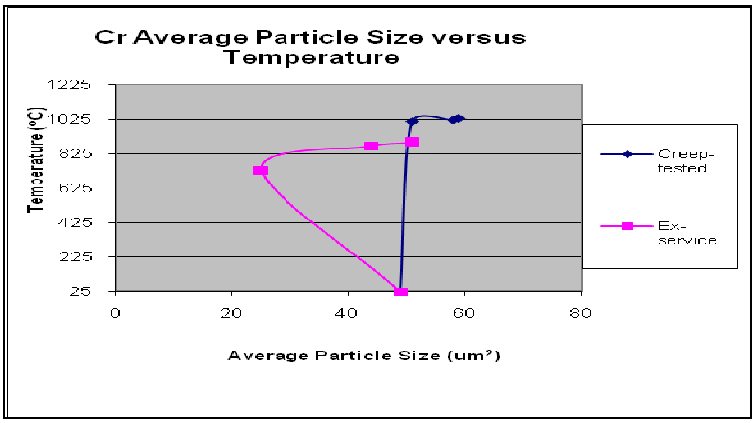

Figure B-1: Graph for Chromium Average Particle Size (µm²) versus Temperature.

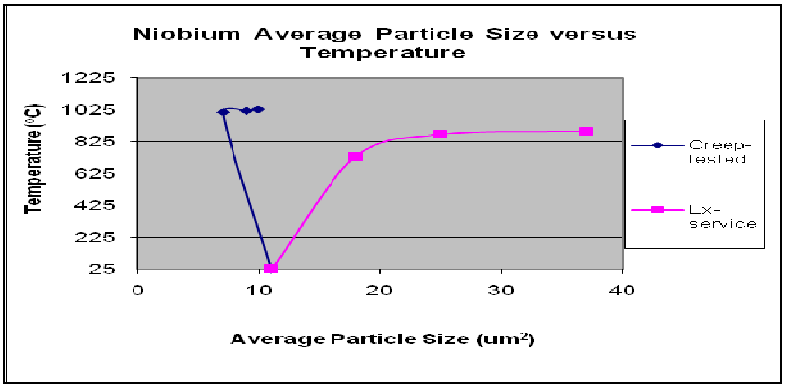

Figure B-2: Graph for Niobium Average Particle Size (µm²) versus Temperature.

APPENDIX C
CONCLUSION

Table C-1: The percent weight, and percent atomic of elements by spot mode.

Sample	Percent Weight (%)			Percentage Atomic (%)		
	Cr K	Nb L	Ti K	Cr K	Nb L	Ti K
O1	72.8	47.7	3.2	53.6	12.1	1.6
A1	75.6	40.9	1.4	60.2	9.6	0.6
A2	75.1	36.3	1.0	60.2	8.4	0.4
A3	74.5	31.7	0.6	60.2	7.1	0.3
K1	76.1	68.4	11.4	63.8	34.9	11.3
K2	63.4	58.7	8.9	53.3	30.8	8.8
K3	25.1	29.6	1.1	22.1	18.3	1.3

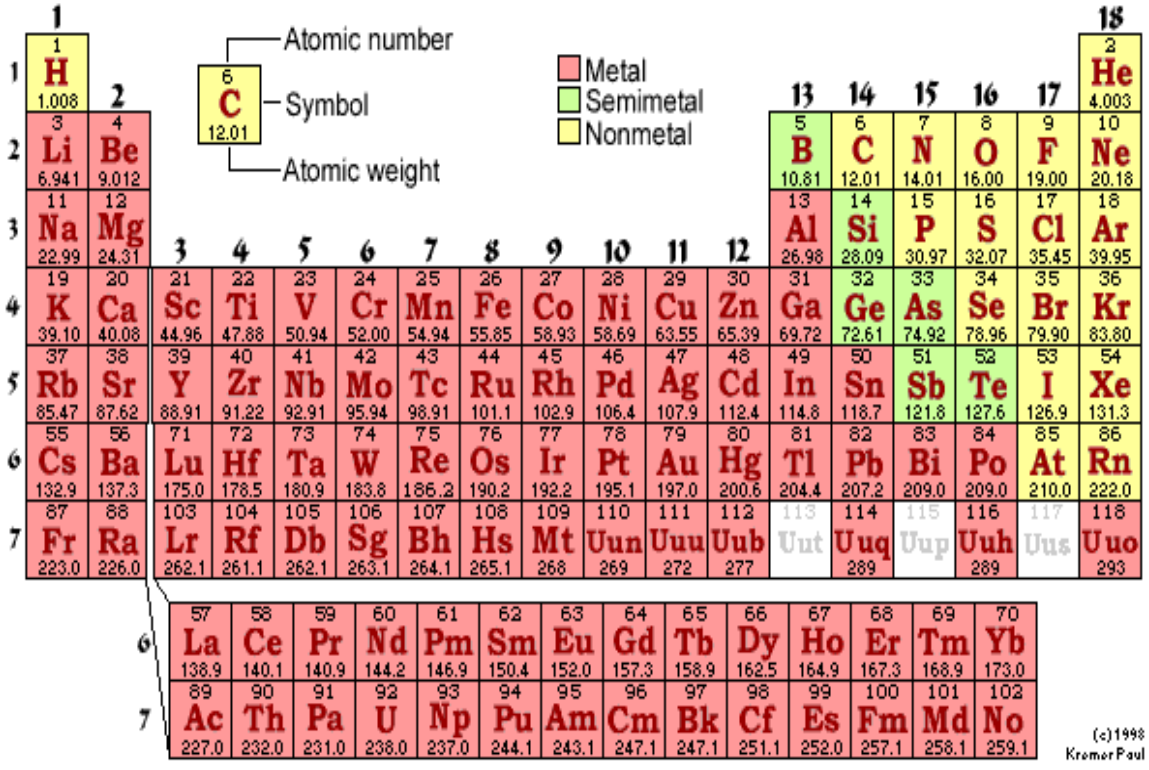

Figure C-1: Periodic table.

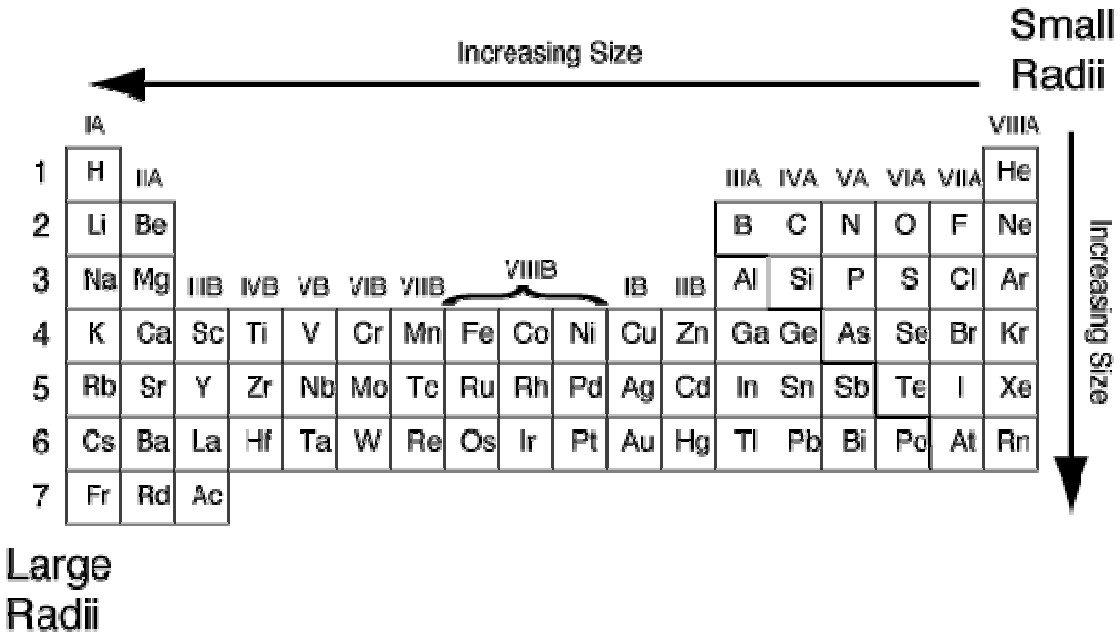

Figure C-2: Periodic table showing atomic radius direction.